J. Fluid Mech. (2022), *vol*. 936, A25, doi:10.1017/jfm.2022.74

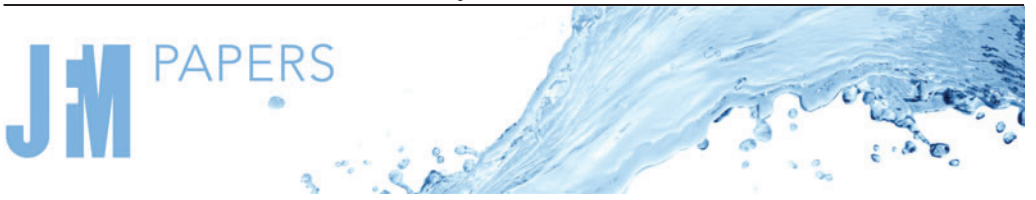

Stationary internal hydraulic jumps

Gregory A. Lawrence[1],† **and Laurence Armi**[2]

[1]Department of Civil Engineering, University of British Columbia, Vancouver, BC, Canada V6T 1Z4

[2]Scripps Institution of Oceanography, La Jolla, CA 92093, USA

(Received 3 July 2021; revised 6 January 2022; accepted 16 January 2022)

This is a theoretical and laboratory study of stationary internal hydraulic jumps. These jumps are rapid transitions between internally supercritical flow, generated by placing a sill on the bed of a horizontal rectangular channel, and internally subcritical flow, generated by installing a downstream contraction. This contraction generates an approximately uniform flow downstream of the jump; thus mimicking barotropically driven two-layer flows, as found in tidally driven flows over underwater sills, and flows over mountain ranges driven by large-scale pressure gradients. Upstream of the jump a train of Kelvin–Helmholtz billows forms on the interface between the layers. Upper layer fluid is entrained into these billows, which are subsequently advected into the lower portion of the jump. These billows are broken down by the turbulence of the jump, and the entrained upper layer fluid is mixed with lower layer fluid. Downstream of the jump the upper layer remains homogeneous, the density step at the interface is weakened, the upper portion of the lower layer is approximately linearly stratified, and the lower portion of the lower layer is undisturbed. This altered density profile is the downstream conjugate state of the jump. When the contraction is narrowed the jump moves upstream and 'drowns' part of the train of billows, reducing the amount of entrainment. Thus, while the jump is responsible for mixing fluid from the upper layer into the lower layer, it is the position of the jump relative to the upstream train of billows that determines the amount of entrainment.

Key words: hydraulic control, topographic effects, shear layers

1. Introduction

Compelling motivation for the study of internal hydraulic jumps is provided by observations in the atmosphere, in oceans and in coastal and inland waters. The 'Bishop Wave' is an internal hydraulic jump several kilometres high that forms on the east side of the Sierra Nevada mountain range (Colson 1952; Armi & Mayr 2011). Similarly, internal hydraulics jumps can dominate the flow in the lee of underwater sills, notably

† Email address for correspondence: lawrence@civil.ubc.ca

the Camarinal Sill in the Strait of Gibraltar (Armi & Farmer 1988; Wesson & Gregg 1994). Internal hydraulic jumps also occur in turbidity currents in oceans, lakes and reservoirs (Garcia & Parker 1989), and when heated water from power plants is discharged into cooling ponds (Wilkinson & Wood 1971). In these, and many other circumstances, considerable entrainment and mixing of fluids of different density is associated with internal hydraulic jumps with important environmental consequences.

There are two main challenges in the study of internal hydraulic jumps. The first is that since internal hydraulic jumps are the rapid transitions matching internally supercritical upstream flows with internally subcritical downstream flows, they cannot by studied in isolation of upstream and downstream conditions. While the same problem exists, and has long been resolved for open channel (free-surface) hydraulic jumps (Bélanger 1828); the problem is more complicated for internal hydraulic jumps, since there are many possible combinations of upstream and downstream conditions. The goal of the present study is to understand stationary internal hydraulic jumps occurring in barotropically driven two-layer flows over a fixed obstacle, as occurs in tidally driven flows over underwater sills, or flows over mountains driven by large-scale pressure gradients. The important characteristics of this configuration are: (i) downstream of the jump the average flow velocity in each of the layers is approximately equal; and (ii) upstream of the jump the lower layer is flowing faster than the upper layer.

Many theoretical studies of internal hydraulic jumps have assumed that mixing between the layers is negligible. In this case many of the techniques developed in the study of free-surface hydraulic jumps in open channel flows can be used. If the flow rate and depth upstream (downstream) of a free-surface jump are known, then the downstream (upstream) conjugate depth is determined by equating the flow force upstream and downstream of the jump (Chow 1959; Henderson 1966). However, in two-layer flows there are two unknowns – the depth of each layer, but only one equation for flow force. Yih & Guha (1955) circumvented this closure problem by considering each layer separately and assuming the pressure on the face of the jump to be hydrostatic. (Chu & Baddour 1977) and (Wood & Simpson 1984) queried the validity of Yih and Guha's model, since it implies that the contracting layer gains energy. They solved the problem by assuming that energy is conserved in the contracting layer. However, (Klemp, Rotunno & Skamarock 1997) postulated that, for some internal bores (moving internal hydraulic jumps) propagating into a stagnant two-layer fluid, the assumption of energy conservation in the expanding layer may be more appropriate. Subsequently, Li & Cummins (1998) proposed a model where energy loss could be assigned arbitrarily to both the layers. Here, we circumvent the closure problem by imposing a uniform velocity profile downstream of the jump, both in our theoretical development and our experimental facility.

The experimental study of internal hydraulic jumps and internal bores was pioneered by Long (1954) and Yih & Guha (1955). Long (1954, 1972) studied the disturbances caused by towing an obstacle along the bottom of a tank filled with two layers of fluid of slightly different density. Yih & Guha (1955) generated internal hydraulic jumps either by discharging dense fluid beneath a less dense stationary ambient, or discharging buoyant fluid over a denser stationary ambient.

Towed obstacle experiments are characterised by internal bores moving upstream and downstream of the obstacle at speeds that are only indirectly related to the towing speed. Considerable attention has been paid to understanding the propagation speed of upstream bores into quiescent fluid, and the relationship between the interface heights upstream and downstream of them (e.g. Li & Cummins 1998; Baines 1995; Borden & Meiburg 2013). Upstream of the bore the layer velocities are equal, and downstream of the bore the upper

layer velocity is greater than the lower layer velocity. This configuration is opposite to that of the stationary internal hydraulic jumps considered in the present study. The result is that the structure of upstream internal bores is fundamentally different than that of stationary internal hydraulic jumps, since there is no shear upstream of the bores (Yeh 1991; Rotunno & Smolarkiewicz 1995; Klemp *et al.* 1997).

The flow structure of internal bores generated downstream of a towed obstacle is similar to that of stationary internal hydraulic jumps: with the lower layer moving faster than the upper layer upstream of the bore, and uniform flow downstream of the bore. Wood & Simpson (1984), Rottman & Simpson (1989) and Kite, Topham & Van Hardenburg (1995) have studied downstream bores in the laboratory, but took no quantitative measurements of entrainment and mixing. Such measurements would be challenging since the instrumentation would need to be towed, mixing would result in a modified density structure after each experiment, and the tank might not be long enough for steady state to be achieved (Long 1954; Baines 1984; Lawrence 1993).

Motivated by engineering applications, where the objective is to either minimise (e.g. Wilkinson 1970; Findikakis & Law 1998) or maximise dilution (e.g. Stefan & Hayakawa 1972); there have been numerous studies similar to Yih & Guha (1955) where inflows were discharged horizontally into stationary deep ambients either as buoyant surface jets (e.g. Wilkinson & Wood 1971; Stefan & Hayakawa 1972; Rajaratnam & Subramanyan 1985; Arita, Jirka & Tamai 1986), or as negatively buoyant bottom jets (e.g. Rajaratnam & Subramanyan 1986; Baddour 1987; Barahmand & Shamsai 2010). These wall jets grow by entraining and mixing significant amounts of ambient fluid, and are often described as entrainment zones. The amount of entrainment and mixing that occurs depends on the length of the entrainment zone, which is sensitive to downstream, as well as upstream, conditions. When a jet grows to the point where it is conjugate to the internally subcritical flow imposed by a downstream control a roller region forms similar to that observed in free-surface hydraulic jumps. This phenomenon is often referred to as a 'density jump' since it is accompanied by a change in the density of the flowing layer. A density jump consists of two distinct zones; an entrainment zone and a roller region (Wilkinson & Wood 1971). Nearly all of the entrainment that occurs in the jump takes place in the entrainment zone.

We distinguish between internal hydraulic jumps and density jumps. The transition from internally supercritical to internally subcritical flow that occurs in an internal hydraulic jump is similar to regular free-surface hydraulic jumps, except that upstream of internal hydraulic jumps there is a shear layer that can generate mixing between the layers. However, in the internal hydraulic jumps studied in the present paper, this shear layer does not penetrate throughout the active layer, and the flow is still approximately two-layered. In density jumps the upstream flow is a wall jet rather than a supercritical two-layer flow, and mixing penetrates throughout the jet.

Theoretical and numerical models have applied various idealisations of the flow upstream and downstream of the phenomena described above. Some have assumed basically the same configuration as Wilkinson & Wood (1971), e.g. Hassid, Regev & Poreh (2007) and Ogden & Helfrich (2020); others have considered flows with no upstream shear between the layers, e.g. Borden, Meiburg & Constantinescu (2012) and Borden & Meiburg (2013); and Thorpe (2010), Thorpe & Li (2014) and Thorpe *et al.* (2018) account for vertical variations in the density and velocity of the lower layer, while assuming a deep stagnant upper layer of uniform density.

In general, neither the configurations adopted in theoretical and numerical studies, nor the experimental approaches of Long (1954) or Yih & Guha (1955), are compatible with

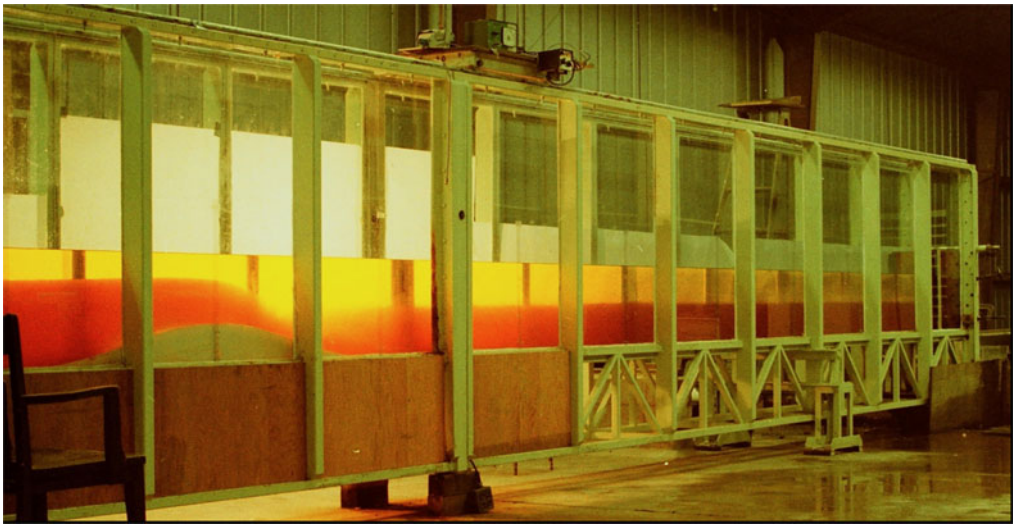

Figure 1. Two-layer flow-through facility. Flow is from left to right, with the lower layer dyed red. An internal hydraulic jump has formed above the lee face of the underwater sill.

the goal of the present study, which is to understand stationary internal hydraulic jumps. Yih & Guha (1955) also had this goal, but commented:

> Experimentally it would be rather difficult and expensive to enable the discharges to vary independently and to realize a stationary jump with two moving layers.

Nevertheless, we were able to generate such flows in the two-layer, flow-through facility shown in figure 1. A crucial component of our experimental set-up is an adjustable downstream contraction, which ensures that downstream of an internal hydraulic jump the flow is internally subcritical flow with approximately the same average velocity in both layers.

In § 2 we summarise the basic theory of hydraulics jumps using a framework that clarifies the similarities between free-surface and internal hydraulic jumps, and aids in the design and interpretation of our experiments. We then extend internal hydraulic theory to facilitate the analysis of our experiments. The results of the laboratory experiments performed to investigate the hydraulics of internal hydraulic jumps are discussed in § 3. Entrainment and mixing associated with internal hydraulic jumps in barotropically driven two-layer flows is addressed in § 4. Our conclusions are presented in § 5.

2. Theory of free-surface and internal hydraulic jumps

Here, we discuss the theoretical and graphical framework (see figures 2 and 3) that we use in the presentation and analysis of our experimental results. We break from tradition by presenting the momentum and energy functions in terms of the appropriate Froude numbers rather than non-dimensional layer thicknesses. The uniform downstream velocity profile eliminates the closure problem recognised by Yih & Guha (1955), and allows us to refine the theory of internal hydraulic jumps (Chu & Baddour 1977; Wood & Simpson 1984). Our analysis is supported by strong analogies between single and two-layer internal hydraulic jumps.

(*a*)

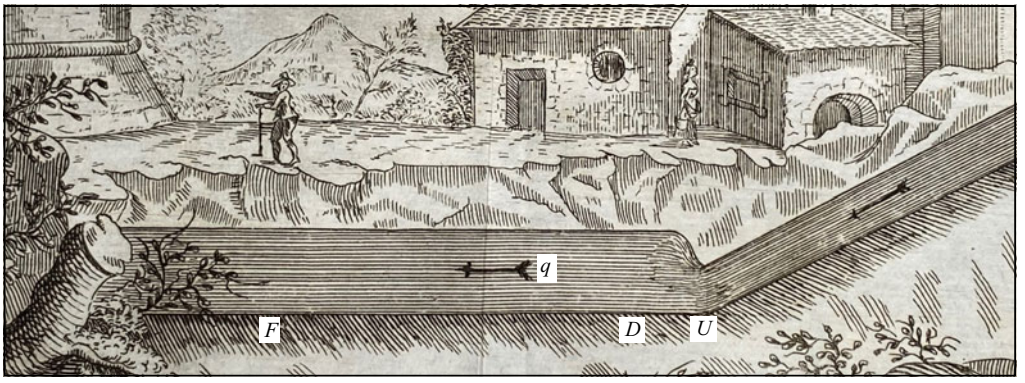

(*b*)

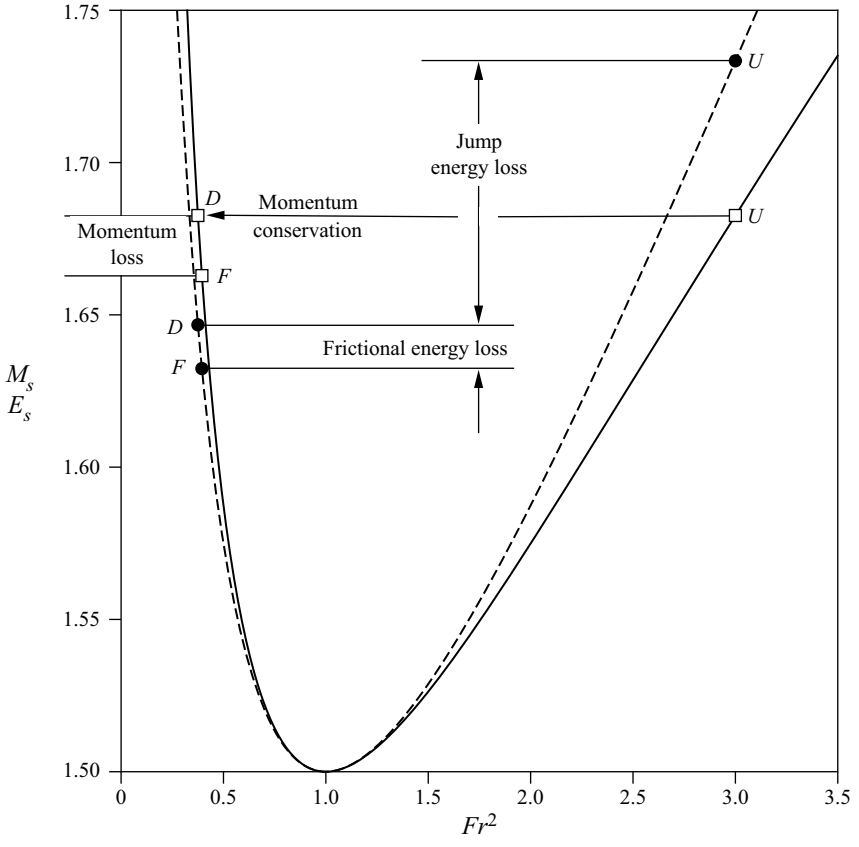

Figure 2. (*a*) Definition sketch adapted from the first known depiction of a hydraulic jump in Guglielmini (1697). (*b*) The dimensionless single-layer energy, E_S (- - - -) and momentum, M_S (——) functions plotted as a function of Fr^2. These curves apply to all single-layer flows in a horizontal, rectangular channel of constant cross-section. The values at points U, D and F have been calculated for the flow depicted in (*a*) where the flow depth downstream of the jump is taken to be double the flow depth upstream of the jump. Values of E_S are represented by solid circles, values of M_S are represented by open squares. From point U, just upstream of the jump, to point D, just downstream of the jump, momentum is assumed to be conserved, but there is considerable energy dissipation. For illustrative purposes the losses of momentum and energy due to friction between D to F are based on an estimated distance between D and F of 10 times the flow depth at D, and a friction factor $f = 0.03$.

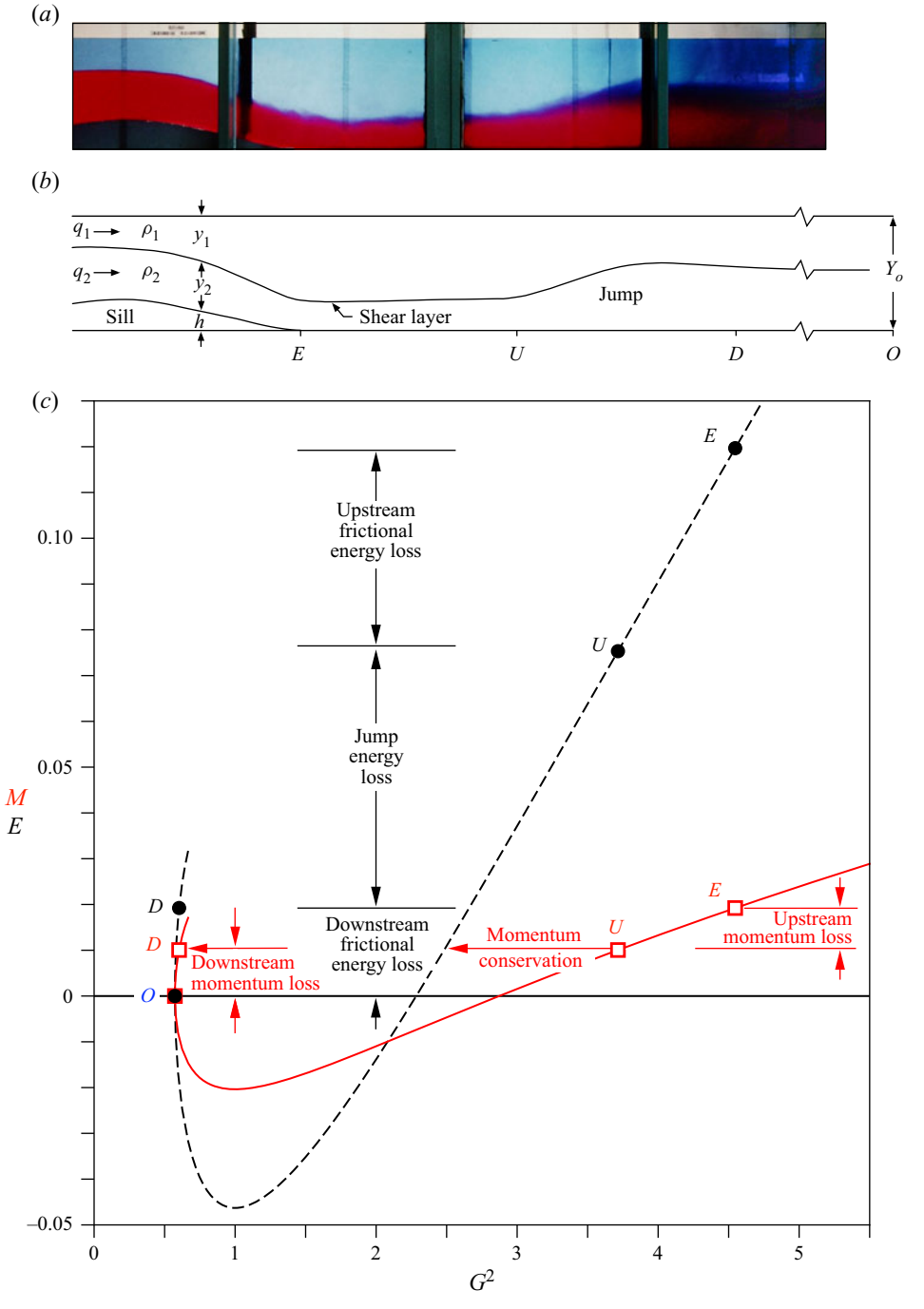

Figure 3. (*a*) Photograph of two-layer flow over an obstacle with a downstream (free) internal hydraulic jump (adapted from Lawrence (1993), figure 6*b*). (*b*) Definition sketch. Here, *E* denotes the end of the sill; *U* and *D* the sections immediately upstream and downstream of the jump, respectively; and *O* denotes the end of the test section, which is at the start of the downstream contraction. (*c*) Energy and momentum plotted as functions of composite Froude number for $r = 0.5$ and $G_0^2 = 0.56$.

Both free-surface and internal hydraulic jumps in a horizontal channel are governed by the momentum, or flow force

$$S = \int_A \left(P + \rho u^2\right) \mathrm{d}A, \tag{2.1}$$

where: A is a cross-section perpendicular to the flow, P is the pressure, ρ is the fluid density and u is the flow velocity. A simple force balance yields

$$\frac{\mathrm{d}S}{\mathrm{d}x} = \int_C \tau(l)\, \mathrm{d}l, \tag{2.2}$$

where x is the flow direction, and τ is the frictional shear stress on the bed and sidewalls of the channel, C.

We make the standard hydraulic assumptions, namely: the pressure is hydrostatic, the density is constant within each layer, the velocity is cross-sectionally uniform within each layer and S is constant across hydraulic jumps (Chow 1959; Henderson 1966).

2.1. *Free-surface hydraulic jumps*

For single-layer flow in a horizontal channel of constant width, W, the basic parameters are the flow depth, y, the volumetric flow rate per unit width, q, the fluid density, ρ, and the gravitational acceleration, g. It is customary in open channel hydraulics (see Henderson (1966), § 2.3) to evaluate (2.1) using the standard hydraulic assumptions, and then non-dimensionalise by $\rho g W y_c^2$, where the critical depth, $y_c = (q^2/g)^{1/3}$, to obtain the non-dimensional, single-layer momentum function

$$M_S = \frac{y'^2}{2} + \frac{1}{y'} = y'^2\left(\frac{1}{2} + Fr^2\right), \tag{2.3a}$$

where $y' = y/y_c$, and the Froude number for single-layer flow

$$Fr^2 \equiv \left(\frac{q^2}{gy^3}\right) = y'^{-3}. \tag{2.3b}$$

Note that, whenever we refer to a Froude number, we refer to the squared quantity, as in (2.3).

A free-surface hydraulic jump is a rapid transition from supercritical upstream flow, $Fr_U^2 > 1$, to subcritical downstream flow, $Fr_D^2 < 1$, where the subscripts $_{\mathrm{U}}$ and $_{\mathrm{D}}$ refer to the conjugate conditions immediately upstream and downstream of the jump.

Assuming negligible friction losses over the length of the jump, and equating the momentum function upstream and downstream of the jump, yields (see Henderson 1966)

$$\frac{y_D}{y_U} = \frac{1}{2}\left(\sqrt{1 + 8Fr_U^2} - 1\right). \tag{2.4}$$

The dimensionless specific energy (Bernoulli constant) for a single-layer flow is given by

$$E_S = y'\left(1 + \frac{Fr^2}{2}\right). \tag{2.5}$$

The loss of specific energy across a free-surface hydraulic jump (see Henderson 1966) is

$$\Delta E_J \equiv E_{SU} - E_{SD} = \frac{(y'_D - y'_U)^3}{4y'_D y'_U}. \tag{2.6}$$

Upstream and downstream of a free-surface hydraulic jump (2.1)–(2.3) give

$$\frac{\mathrm{d}M_S}{\mathrm{d}x'} = -\frac{f}{8}\frac{y}{R_h} Fr^2 y', \tag{2.7}$$

where $x' = x/y_c$, the hydraulic radius, $R_h \equiv A/P = Wy/(W + 2y)$, where A is the cross-sectional area of the channel and P is its wetted perimeter. Methods for determining the Darcy–Weisbach friction factor, f, are given in Chow (1959) and Finnemore & Franzini (2002).

The above concepts are illustrated in figure 2(*b*) by plotting M_S and E_S vs Fr^2 for the flow depicted in figure 2(*a*). In this flow $y_D/y_U \approx 2$, and (2.3*a*) and (2.4) give the conjugate states $Fr_U^2 = 3$ and $Fr_D^2 = 3/8$. Across the jump momentum is assumed constant, and (2.6) gives $\Delta E_J = 0.087$. Downstream of the jump, between D and F, friction results in a gradual decrease in M_S, in accordance with (2.7).

While (2.4) allows us to calculate the relationship between upstream and downstream conditions, we must emphasise a point made by Henderson (1966, p. 69) that is central to the present study:

> But it is most important to realize that this downstream depth is caused not by the upstream conditions but by some control acting further downstream. If this control produces the required depth y_2, a jump will form; otherwise, it will not.

Consider the flow depicted in figure 2(*a*) where the jump is located at a transition in bed slope (a transitional jump). If the height of a downstream weir (not visible) were lowered, so that the flow depth and momentum function at D were reduced, then the momentum function at D would be less than that at U. To redress this imbalance the position of the jump would move downstream (a free jump), exposing a reach of supercritical flow that, due to friction, would reduce the momentum so that that the flow conditions upstream and downstream of the jump were again conjugate to each other. On the other hand, if the downstream depth were increased the position of the jump would move upstream, creating a drowned hydraulic jump (see Chow 1959), and the analysis would need to be modified to account for the sloping bed upstream of U.

2.2. *Momentum and energy functions for two-layer flows*

Now we follow the procedure presented above to derive momentum and energy functions for two-layer flows. The experiment depicted in figure 3, will be used to provide context. For two-layer flow in a channel of constant width, W, the basic flow parameters are: the layer depths, y_i, where the subscripts $i = 1, 2$ refer to the upper and lower layers, respectively; the volumetric flow rate per unit width of each layer, q_i; the flow rate ratio, $r = q_2/q$, where $q = q_1 + q_2$; and the reduced gravitational acceleration, $g' = \varepsilon g$, where $\varepsilon = (\rho_2 - \rho_1)/\rho_2$. In the present study we assume $\varepsilon \ll 1$. The total flow depth, $Y = y_1 + y_2 + h$, where h is the local height of the sill.

For two-layer flows in a horizontal channel of constant width (2.1) becomes

$$S = \int_0^{y_2} (P_2 + \rho_2 u_2^2) W \,\mathrm{d}z + \int_{y_2}^{Y} (P_1 + \rho_1 u_1^2) W \,\mathrm{d}z. \tag{2.8}$$

To evaluate (2.8), Chu & Baddour (1977) and Wood & Simpson (1984) assumed that the pressure is hydrostatic, and that within each layer the density is constant and the velocity is cross-sectionally uniform. After dividing by $\rho g' W Y^2$, they obtained to $O(\varepsilon)$

$$S_T = \frac{1}{2\varepsilon} + {y_2'}^2\left(\frac{1}{2} + F_2^2\right) + {y_1'}^2 F_1^2, \tag{2.9}$$

where $y_i' = y_i/Y$. For single-layer flows there exists a critical depth, y_c, which we used for non-dimensionalisation in § 2.1. No simple critical depth exists for two-layer flows, and we use the total depth, Y, for the non-dimensionalisation. The densimetric Froude number

$$F_i^2 = \frac{q_i^2}{g' y_i^3}. \tag{2.10}$$

Note again, that whenever we refer to a Froude number, we refer to the squared quantity. Note also, that the composite Froude number (Armi 1986),

$$G^2 = F_1^2 + F_2^2 - \varepsilon F_1^2 F_2^2, \tag{2.11}$$

rather than the densimetric Froude number, is commonly used to describe the criticality of two-layer flows (see Appendix A for details).

In density jumps the assumptions of constant density and uniform velocity within each layer are not satisfied. Wilkinson & Wood (1971) and others have relaxed these assumptions by using correction factors in their analyses of density jumps. However, the internal hydraulic jumps that we investigate in the present paper cause far less disruption to the flow than density jumps, and we do not incorporate correction factors into our analysis of the hydraulics of two-layer flows. This allows us to focus on understanding the processes that govern the entrainment and mixing associated with internal hydraulic jumps.

As it stands (2.9) is not particularly useful, since the first term on the right-hand side is $O(\varepsilon^{-1})$ times as large as the other terms. Following Chu & Baddour (1977) and Wood & Simpson (1984), we eliminate this term by assuming that the upper layer energy, $E_1 = \rho_1 g Y + \rho_1 u_1^2/2$, is constant. The resulting non-dimensional momentum function for two-layer flows to $O(\varepsilon)$ is

$$M_T \equiv S_T - \frac{1}{2\varepsilon}\left(\frac{E_1}{\rho_1 g Y}\right)^2 = {y_2'}^2\left(\frac{1}{2} + F_2^2\right) + \frac{1}{2}(y_1' - y_2')y_1' F_1^2. \tag{2.12}$$

To $O(\varepsilon)$ (2.12) is the same as those obtained by Chu & Baddour (1977) and Wood & Simpson (1984). Note that if the upper layer is passive, i.e. if $F_1^2 \ll F_2^2$, (2.12) has the same form as (2.3*a*), its single-layer counterpart.

While our focus is on variations in the momentum function, since they determine the position of internal hydraulic jumps, it is also informative to consider variations in the two-layer energy function, defined by Baddour & Abbink (1983) and others, as

$$E_T \equiv \frac{E_2 - E_1}{\rho_2 g' Y} = y_2'\left(1 + \frac{1}{2}F_2^2\right) - \frac{1}{2}y_1' F_1^2. \tag{2.13}$$

As in the case of the momentum function, if the upper layer is passive, i.e. when $F_1^2 \ll F_2^2$, (2.13) has the same form as (2.5), its single-layer counterpart.

2.3. *Internal hydraulic jumps in barotropically driven two-layer flows*

We study two-layer flow in a horizontal, rectangular channel, as depicted in figure 3. An internally supercritical flow downstream of the crest of a sill is followed by an

internal hydraulic jump that transitions to an internally subcritical flow. We model a barotropically driven two-layer flow by installing a downstream width contraction, which imposes an approximately uniform velocity profile at the downstream end of the channel (see Appendix A for details). The uniform downstream velocity profile eliminates the closure problem recognised by Yih & Guha (1955), and allows us to refine the theory of internal hydraulic jumps.

Here, we derive the appropriate momentum and energy functions needed to analyse this configuration. Wood (1968) and Armi (1986) show that, to $O(\varepsilon)$

$$u_{1o} = u_{2o} = \frac{q}{Y_o}, \tag{2.14}$$

where the subscript 'o' designates conditions at the end of the test section; i.e. at the start of the downstream contraction. Substituting (2.14) into (2.11), yields

$$G_o^2 = \frac{q^2}{g' r(1-r) Y_o^3}, \tag{2.15}$$

where the two-dimensional flow rate, $q = q_1 + q_2$; the total depth, $Y_0 = y_{1o} + y_{2o}$, and the flow rate ratio

$$r = \frac{q_2}{q}. \tag{2.16}$$

The present study investigates flows with $G_0^2 < 1$. At low flow rates, the flow is internally subcritical throughout the channel with only a slight depression in the interface level over the sill. This case is not of interest in the present study, since there is no internal hydraulic jump. At sufficiently higher flow rates the flow will become internally supercritical on the lee face of the sill; in such flows an internal hydraulic jump will form between the crest of the sill and the downstream contraction. Lawrence (1993) has shown that G_0^2 and r, in conjunction with the non-dimensional obstacle height, $\beta_m = h_m/Y_0$, where h_m is the maximum height of the obstacle, determine which of these cases occurs. The values of G_0^2, r and β_m for the experiments performed in the present study are given in table 1.

Under the assumption of uniform flow at the downstream end of the channel, $y_{2o} = r$, and (2.12) simplifies to

$$M_{To} = \tfrac{1}{2}\{r^2 + r(1-r)G_0^2\}. \tag{2.17}$$

To best illustrate the properties of internal hydraulic jumps, we define the non-dimensional two-layer momentum function

$$M \equiv M_T - M_{To} = \frac{1}{2}\eta\,(2r+\eta) + r(1-r)G_0^2 \left\{ \frac{r^2}{r+\eta} + \frac{\left(\frac{1}{2} - r - \eta\right)(1-r)^2}{(1-r-\eta)^2} - \frac{1}{2} \right\}, \tag{2.18}$$

where $\eta = y_2' - r$.

Applying (2.2) to gradually varying two-layer flow in a horizontal channel yields

$$\frac{\mathrm{d}M}{\mathrm{d}x'} = -\frac{f_1}{8}\left(\frac{y_1}{R_{h_1}}\right) F_1^2 y_1' - \frac{f_2}{8}\left(\frac{y_2}{R_{h_2}}\right) F_2^2 y_2', \tag{2.19}$$

where f_1 and $R_{h_1} = W/2$, and f_2 and $R_{h_2} = Wy_2/(W + 2y_2)$, are the friction factors and hydraulic radii for the upper and lower layers, respectively. Equation (2.19) is analogous

https://doi.org/10.1017/jfm.2022.74 Published online by Cambridge University Press

	Series A					Series B							
Exp. #	1	2	3	4	5	6	7	8	9	10	11	12	13
q_1	190	190	190	190	190	217	217	217	217	134	213	101	204
q_2	95	95	95	95	95	145	145	145	145	67	142	99	204
h_m	8.0	8.0	8.0	8.0	8.0	8.0	8.0	8.0	8.0	8.0	8.0	15	15
W_{min}	1.4	1.6	1.8	2.0	2.2	1.2	1.6	1.8	2.2	1.4	1.8	1.2	1.9
Y	44.1	39.8	38.1	34.9	33.9	58.0	48.8	44.4	39.0	37.3	42.4	40.2	46.5
g'	18.3	17.6	17.8	17.8	17.7	20.0	19.7	19.5	19.9	9.0	18.9	8.0	14.8
r	0.33	0.33	0.33	0.33	0.33	0.40	0.40	0.40	0.40	0.33	0.40	0.50	0.50
β_m	0.18	0.20	0.21	0.23	0.24	0.14	0.16	0.18	0.21	0.21	0.19	0.37	0.32
G_0^2	0.23	0.33	0.37	0.48	0.53	0.14	0.24	0.32	0.46	0.39	0.36	0.31	0.45
F_{1E}^2	*0.03*	*0.05*	0.05	0.07	0.08	*0.02*	*0.03*	*0.04*	0.06	0.05	*0.05*	0.03	*0.05*
F_{2E}^2	*7.5*	*7.1*	7.0	6.4	6.1	*6.4*	*6.1*	*5.9*	5.4	6.9	*5.8*	7.0	*4.4*
G_E^2	*7.6*	*7.2*	7.0	6.5	6.2	*6.4*	*6.1*	*5.9*	5.4	7.0	*5.8*	7.0	*4.5*
$F_{\Delta E}^2$	*4.8*	*4.2*	4.0	3.3	3.0	*4.5*	*4.0*	*3.6*	2.9	3.9	*3.4*	4.9	*2.7*
Re^*	1100	1000	1000	1000	900	1300	1300	1200	1100	700	1100	900	1100
L_T	717	717	717	717	717	788	788	788	788	715	780	740	740
M_E	*−0.003*	*0.007*	0.011	0.019	0.021	*−0.030*	*−0.012*	*−0.001*	0.014	0.012	*0.005*	—	—
M_f	0.006	0.008	0.009	0.011	0.012	0.004	0.006	0.008	0.011	0.010	0.008	0.010	0.011
x_j/L_S	0.60	0.70	0.90	2.69	2.79	0.26	0.46	0.66	3.44	1.79	0.80	0.64	0.95
$M_f - M_E$	*0.009*	*0.001*	−0.002	−0.008	−0.008	*0.034*	*0.018*	*0.009*	−0.003	−0.002	*0.003*	—	—
Jump Type	Drowned	Drowned	Trans.	Free	Free	Drowned	Drowned	Drowned	Free	Free	Drowned	Trans.	Drowned

Table 1. Experimental data. Note that all dimensional quantities are in cgs units. The values given for drowned jumps at the end of the sill (subscript 'E') are calculated assuming there is no drowned jump and written in italics; M_E was not calculated for Exps. 12 and 13 because the flow over the sill was subject to substantial non-hydrostatic effects (Zhu & Lawrence 1998).

to (2.7), the corresponding single-layer result. In our experiments the walls of the channel can be assumed to be smooth, in which case

$$f_i = 0.223 Re_{h_i}^{-1/4}, \tag{2.20}$$

where the hydraulic Reynolds number, $Re_{h_i} = u_i R_{h_i}/\nu$, $i = 1, 2$ (see Chow 1959). Note that f_1 and f_2 are the friction factors due to shear on the bed and sidewalls of the channel; they are not interfacial friction factors. Interfacial friction does not play a role in the calculation of M.

Following our approach for momentum, we define the non-dimensional two-layer energy function

$$E \equiv E_T - E_{To} = \eta + \frac{1}{2} r\,(1-r)\,G_0^2 \left\{ \left[\frac{r}{r+\eta} \right]^2 - \left[\frac{(1-r)}{(1-r-\eta)} \right]^2 \right\}, \tag{2.21}$$

see Lawrence (1993). Note that, for convenience, we have defined the two-layer momentum and energy functions so that, at the downstream end of the channel where $\eta = 0$, (2.18) and (2.21) give $M = 0$ and $E = 0$, respectively.

The above concepts are illustrated by the two-layer flow examined in figure 3. This flow has been visualised in figure 3(*a*) by dyeing the lower layer red and the upper layer blue, so that mixing between the layers appears purple. Note that mixed fluid is present in a shear layer upstream of the jump, as well as in the jump itself. This mixing can be ignored for the moment, but will be examined in detail in § 4. A definition sketch for the flow is presented in figure 3(*b*). The variation of M and E with G^2 is presented in figure 3(*c*). While there are differences, this plot is very similar to its single-layer counterpart presented in figure 2(*b*), as are the basic causes of variation in the momentum and energy.

Let us consider the changes in M and E from the end of the sill (E) to end of the test section (O). From E until the start of the jump (U) the flow is internally supercritical with an active lower layer, i.e. $F_2^2 \gg F_1^2$. The values of M and E gradually decrease due to friction on the bed and sidewalls of the channel. From U to the downstream end of the jump (D) momentum loss is negligible, but there is a considerable loss of energy. In the internally subcritical reach from D to O, M and E gradually decrease, as in the shear layer upstream of the jump, but the rate of decrease is less than in the shear layer, since the lower layer velocity is less, figure 3(*b*).

Hydraulic jumps can form: downstream of the obstacle (free jumps); between the crest and downstream end of the sill (drowned jumps); or the start of the jump may occur at the end of the sill (transitional jumps). The flow of Guglielmini (1697), shown in figure 2, is an example of a transitional free-surface hydraulic jump. For a transitional jump to form, M_E, the flow's momentum at the end of the sill, should match M_f, the loss of momentum due to friction on the sidewalls and bed of the flume in the internally subcritical flow between the end of the sill and the end of the test section. If the hydraulic assumptions hold, M_E can be estimated using the approach outlined in Lawrence (1993) and M_f can be estimated using (2.19). The jump type can be predicted according to the following:

$$\text{If} \quad \begin{cases} M_E > M_f & \text{a free jump occurs,} \\ M_E \approx M_f & \text{a transitional jump occurs,} \\ M_E < M_f & \text{a drowned jump occurs.} \end{cases} \tag{2.22}$$

While M_E and M_f are small quantities that are difficult to evaluate experimentally, (2.22) serves as a useful guide to the location of internal hydraulic jumps.

3. Experiments on the hydraulics of internal hydraulic jumps

Thirteen experiments were performed to better understand the internal hydraulic jumps that form downstream of a two-dimensional fixed obstacle in steady, barotropically driven two-layer flow. The flow parameters and important results for each of these experiments are given in table 1. The experiments were performed in the facility shown in figure 3. The experimental set-up and procedures will be discussed briefly, for further details see Lawrence (1985, 1993).

Fresh and salt water were introduced separately into a 3.05 m wide chamber at the upstream end of the flow facility (figure 4*a,b*). Fresh water was drawn from the mains into a constant head tank, and salt water was pumped from San Francisco Bay into a 370 m^3 pond, and then into a second constant head tank. The maximum discharge from each of the head tanks was 10^{-2} m^3 s^{-1}, so that the experiment could be run at maximum discharge for approximately 10 hours before the saltwater pond was emptied. The discharges were measured to within ± 2 % with orifice meters (figure 4*b*). The two-dimensional flow rates in the experiments were in the range $200 \leq q \leq 408\,cm^2\,s^{-1}$, yielding bulk Reynolds numbers, $Re = q/\nu = 2.0\text{–}4.1 \times 10^4$, where ν is the kinematic viscosity of water. The density of each fluid was measured using a hydrometer that enabled the relative density difference to be determined to within ± 0.0003. The relative density differences of the experiments were in the range $0.0082 \leq \boldsymbol{\varepsilon} \leq 0.0204$. Note that up to 10 000 kg of salt passed through the facility during a 10 h series of experiments.

Perforated pipes discharged the inflows evenly across the width of the inflow chamber, see figure 4(*c*). A splitter plate installed between these pipes was hinged so that it could be adjusted to match the interface level imposed from downstream. Synthetic horsehair matting was installed above and below the splitter plate, and a fine mesh screen was placed perpendicular to the flow, to reduce the magnitude of turbulent fluctuations and minimise upstream mixing between the two layers. The velocity and density profiles were measured at selected locations along the length of the channel using a miniature propellor meter and a conductivity probe. The glass-sided flume was 12.9 m long, 37.6 cm wide and the depth of flow, Y, varied from 33.9 to 58.0 cm with a measurement error of approximately ± 0.2 cm.

The plan view of the facility (figure 4*b*) shows that after passing through the inflow section, into the constant width flume, the flow passes over an obstacle spanning the width of the flume placed approximately half-way along the flume. An internal hydraulic jump forms downstream of the crest of the obstacle to match the internally subcritical flow imposed by the virtual control in the adjustable downstream contraction (figure 4*d*). The obstacle shape was built to satisfy the equation

$$h\,(x) = h_m \cos^2\left(\frac{\pi}{2}\frac{x}{L_s}\right) \tag{3.1}$$

to within ± 2 mm over the domain $|x/L_s| \leq 1$, where: the maximum height of the obstacle, $h_m = 8.0$ cm for all experiments (except Exps. 13 and 14, with $h_m = 15.0$ cm); and the half-width of the sill, $L_s = 2\pi h_m$. The downstream contraction was 50 cm long, with an exit width, W_{min}, that was varied from 1.2 to 2.2 cm over the course of the experiments. The total flow depth only decreased visibly as $Fr^2 \to 1$, in the last few centimetres before the exiting the downstream contraction (figure 4*a*). The flow discharged freely from the contraction into a sump.

By analogy with the experiments of Wilkinson & Wood (1971), we assumed that the mixing associated with internal hydraulic jumps in our facility would depend on their position with respect to the obstacle. To test this assumption, we conducted two series of

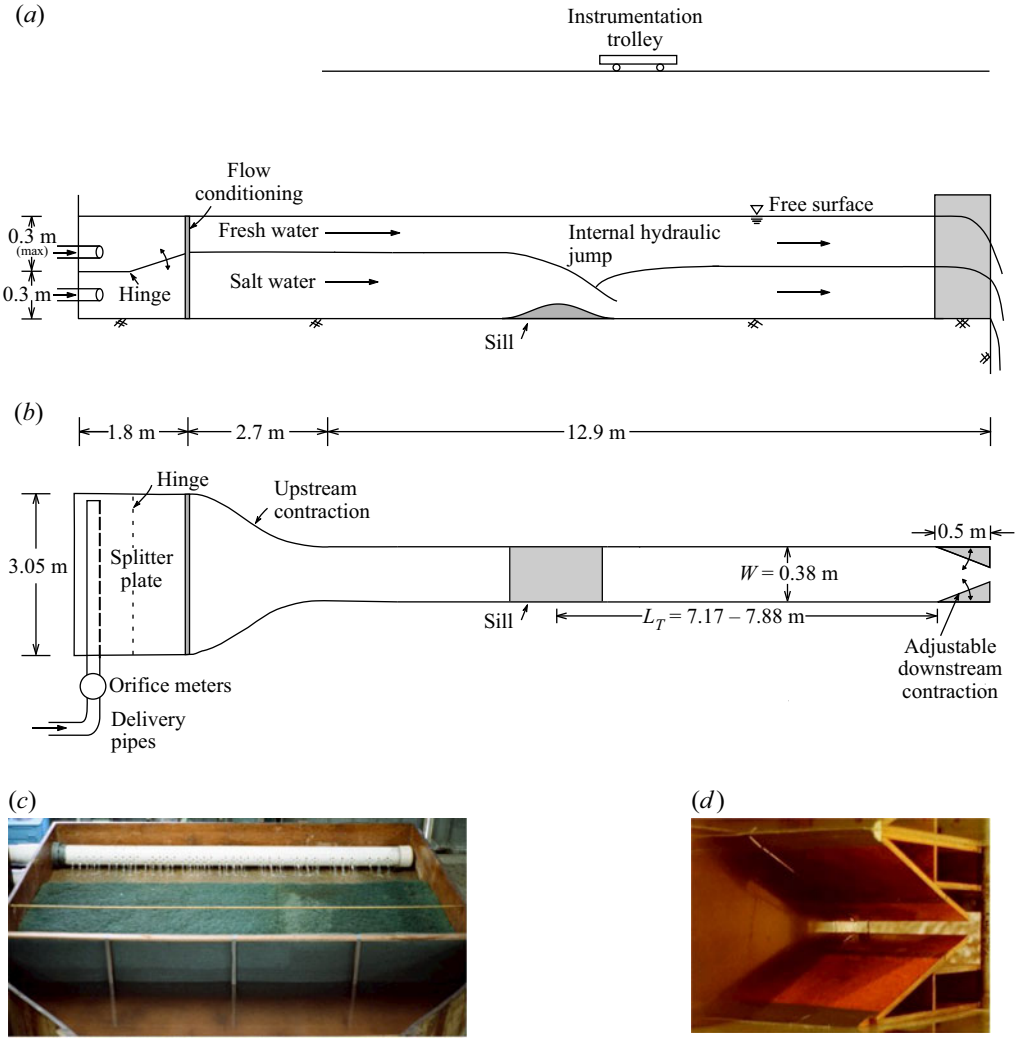

Figure 4. Details of the two-layer flow facility. (*a*) Elevation and (*b*) plan views (not to scale). (*c*) Photographs of inflow section and (*d*) adjustable downstream contraction. The minimum width of the adjustable downstream contraction is varied between 1.2 and 2.2 cm. The length of the test section, L_T, varied depending on the location of the sill.

experiments, Series A (Exps. 1–5) and Series B (Exps. 6–9). Each series of experiments took about 10 hours to complete, during which time the flow rate of each layer remained almost constant, as did the densities of each layer, see table 1. Only the exit width of the downstream contraction, W_{min}, was adjusted from experiment to experiment within each Series. Once W_{min} was set, we waited for approximately 1 hour to ensure that the free surface elevation and jump position were at steady state. Measurements of interfacial elevation, and profiles of velocity and density were taken, and the flow was visualised with dye and photographed. Then the width of the downstream contraction was increased and the process repeated. In each series of experiments the range of widths for the downstream contraction, and consequently the range of flow depths, was chosen such that free, transitional and drowned jumps formed.

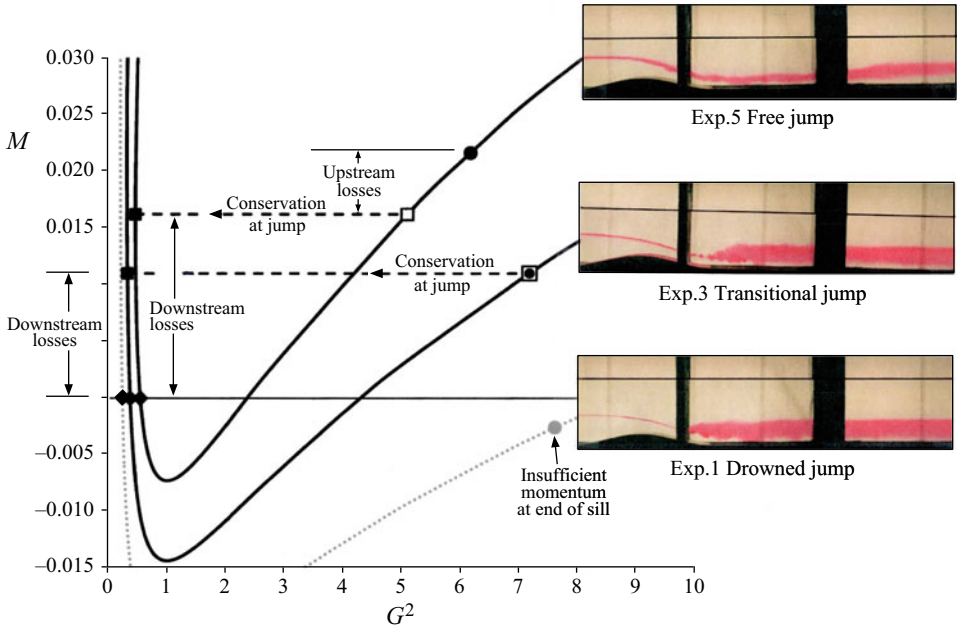

Figure 5. Momentum function plotted as a function of G^2 for Exps. 1, 3 and 5 together with photographs of these experiments. Solid circles indicate conditions at the end of the sill, open squares indicate conditions at the start of the jump, solid squares indicate conditions at the end of the jump and diamonds indicate conditions at the end of the channel. The experiments were performed on the same day and the upstream inflow rates and densities were constant (see table 1). In Exp. 1 the total depth, $Y = 44.1$ cm, the exit width of the downstream contraction, $W_{min} = 1.4$ cm and a drowned jump formed over the lee face of the sill. In Exp. 3 W_{min} was increased to 1.8 cm, causing the total depth to decrease to 38.1 cm, and a transitional jump formed at the end of the sill. In Exp. 5, $W_{min} = 2.2$, $Y = 33.7$ cm, and a free jump formed downstream of the sill. Red dye injected upstream at the density interface helps visualise the flow.

To further understand the processes of mixing and entrainment we conducted four additional experiments. Experiments 10 and 11 were performed with the centreline of the channel illuminated by a sheet of laser light. This enabled us to observe the details of the flow while minimising sidewall effects. Exp. 12 was conducted to obtain high-resolution vertical profiles of conductivity upstream of the obstacle, between the obstacle and the jump, and downstream of the jump. Finally, Exp. 13 was conducted to obtain time series of conductivity above, below and at several locations within a jump.

3.1. *Series of experiments to verify two-layer hydraulic theory (Exps. 1–5)*

The Series A experiments were performed with $h_m = 8.0$ cm, $q_1 = 190$, $q_2 = 95\,\mathrm{cm^2\,s^{-1}}$ and $g' \approx 18\,\mathrm{cm\,s^2}$ (see table 1) The width of the downstream contraction was set at 1.4 cm for Exp. 1 and increased to 1.6, 1.8, 2.0 and 2.2 cm for Exps. 2–5, respectively. The upstream flow rate ratio was fixed at $r = 0.33$, and the other governing non-dimensional parameters, G_0^2 and β_m, varied as the free surface elevation dropped (see figure 5 and table 1). We use the theory presented in Lawrence (1993) to predict the momentum at the end of the sill, M_E, and integrate (2.19) to calculate M_f. In figure 5(*a*) the M vs G^2 curves for $r = 0.33$ are plotted for flows with a drowned jump (Exp. 1), a transitional jump (Exp. 3) and a free jump (Exp. 5). These curves are used in conjunction with photographs of the experiments (figure 5*b–d*) to explain the dynamics of the flow in each of these experiments.

Exp.	x (m)	q_{12}	q_{21}	q_{ENT}	ψ_{INT}
6	–1.5	0.006	0.004	0.002	0.402
6	4.5	0.014	0.004	0.009	0.409
7	4.5	0.023	0.004	0.019	0.419
8	4.5	0.035	0.004	0.031	0.431
9	4.5	0.040	0.013	0.027	0.427

Table 2. Entrainment fluxes in Experiments 6–9.

In Exp. 1 ($M_E = -0.003,\ M_f = 0.006$) a drowned internal hydraulic jump formed midway down the lee face of the sill, in accordance with (2.22). Note that in this experiment $M_E < 0$, indicating that a drowned jump would have formed even if there were no frictional momentum loss (see figure 5). A thin filament of red dye injected at the interface between the two layers at the entrance to the flume remained undisturbed until it reached the drowned jump. The dye was then entrained and mixed into the jump, highlighting the location of the jump, and the disturbed portion of the lower layer, which persisted until the end of the flume. A train of Kelvin–Helmholtz billows is observed underneath the nose of the jump, and the lower portion of the lower layer remained undisturbed. Experiments performed to investigate Kelvin–Helmholtz billowing and the entrainment and mixing that it causes are presented in § 4. Note that in all our experiments, the increase in the flow rate ratio caused by this entrainment and mixing is less than 10 % (see table 2), which does not warrant replotting the illustrative M vs G^2 curves in figure 5. This observation is in contrast with the higher internal Froude number density jumps of Wilkinson & Wood (1971) in which substantial mixing and entrainment occurred in the jet upstream of the jump and extended throughout the lower layer. The reasons for this difference are discussed in § 4.

In Exps. 2–5 both M_E and M_f increased as the downstream contraction, W_{min}, was progressively opened decreasing the total depth of flow, Y (table 1). However, M_E increased more rapidly than M_f and, as a consequence, the jump moved progressively further downstream. In Exp. 2 ($M_E = 0.007,\ M_f = 0.008$) the jump remained drowned, since $M_E < M_f$, but moved further down the lee face of the obstacle. Otherwise, Exp. 2 was very similar to Exp. 1. In Exp. 3 ($M_E = 0.011,\ M_f = 0.009$) a transitional jump formed at the end of the sill, since $M_E \approx M_f$. In this experiment a train of Kelvin–Helmholtz billows formed on the interface upstream of the jump (figure 5).

Free jumps formed in Exps. 4 and 5, respectively, since in both cases $M_E > M_f$ (see figure 5 and table 1). In these experiments the decrease in M due to friction is greater than M_f, since M_f is calculated assuming subcritical flow; whereas, in these experiments the rate of frictional loss in the supercritical flow between the end of the sill and the jump is greater, in accordance with (2.19). From the end of the sill until the jump, the lower layer depth increases gradually until the lower layer depth, y_{2U}, and the composite internal Froude number just upstream of the jump, G^2_U, are conjugate to the depth, y_{2D}, and the composite internal Froude number, G^2_D, downstream of the jump (figure 5). The free jumps in Exps. 5 and 6 are weaker than the drowned and transitional jumps (Exps. 2–4), because the composite Froude number downstream of the jump is higher.

In all of the Series A experiments, dye injected at the interface upstream of the sill was entrained into the jump, irrespective of the position of the jump. The jump consists of interfacial fluid mixed with lower layer fluid. No interfacial fluid made its way into the upper layer, nor did it enter the lower portion of the lower layer.

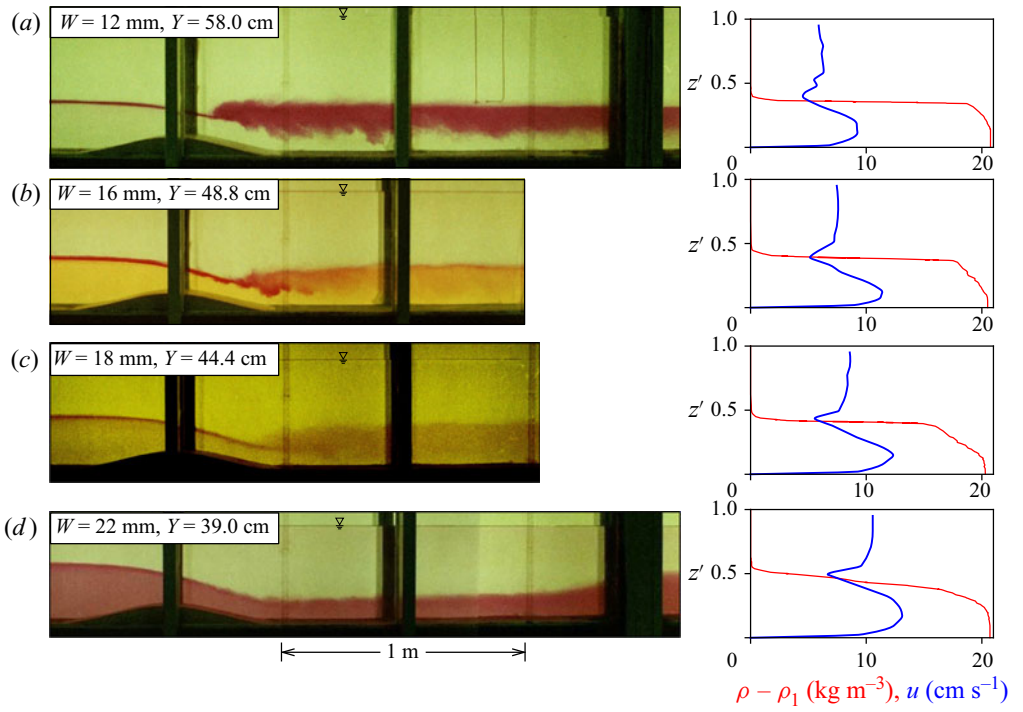

Figure 6. (*a–d*) Photographs of Exps. 6–9 showing the effect of varying the total depth on the position of the jump, and the velocity and density profiles 5.5 m downstream of the crest of the sill. All the experiments were performed on the same day with the same flow rates and densities (see table 1). The conductivity probe and micro-propeller meter are visible just above the interface in (*a*).

3.2. *Series of experiments to investigate impact of jump position on entrainment and mixing (Exps. 6–9)*

Series B was performed with $h_m = 8.0\,\text{cm}$, $q_1 = 217$, $q_2 = 145\,\text{cm}^2\,\text{s}^{-1}$ and $g' \approx 20\,\text{cm}\,\text{s}^{-2}$. The width of the downstream contraction was set at 1.2 cm for Exp. 6 and increased to 1.6, 1.8 and 2.2 cm for Exps. 7–9, respectively. In Series B, $r = 0.40$, whereas in Series A, $r = 0.33$. Otherwise, the primary difference is that in Series B velocity and density profiles were measured downstream of the jump (figure 6*a–d*) to quantify modifications to the flow caused by internal hydraulic jumps. The velocity profiles were not continuous, they were obtained by holding the propellor meter fixed for a period of 40 s at a series of vertical positions.

In Exp. 6 a drowned jump formed just downstream of the crest of the obstacle (figure 6*a*), as expected since $M_E < M_f$. The density profile confirms the visual observation of entrainment of upper layer fluid into upper portion of the lower layer (figure 6*a*). The velocity profile is almost uniform, although a velocity deficit (wake), due to the stationary jump and the divergence of the upper layer over the lee face of the sill, is still evident 5.4 m downstream of the nose of the jump. This wake is likely to be less pronounced, but still present, in the downstream contraction which starts 7.7 m downstream of the nose of the jump. Similar wakes were observed in Exps. 7–9 (figure 6*b–d*).

As in the Series A experiments, when the downstream contraction was opened the water level dropped, and the jump moved progressively further downstream (figure 6*a–d*). In each case a different downstream density profile resulted. In the experiments with drowned

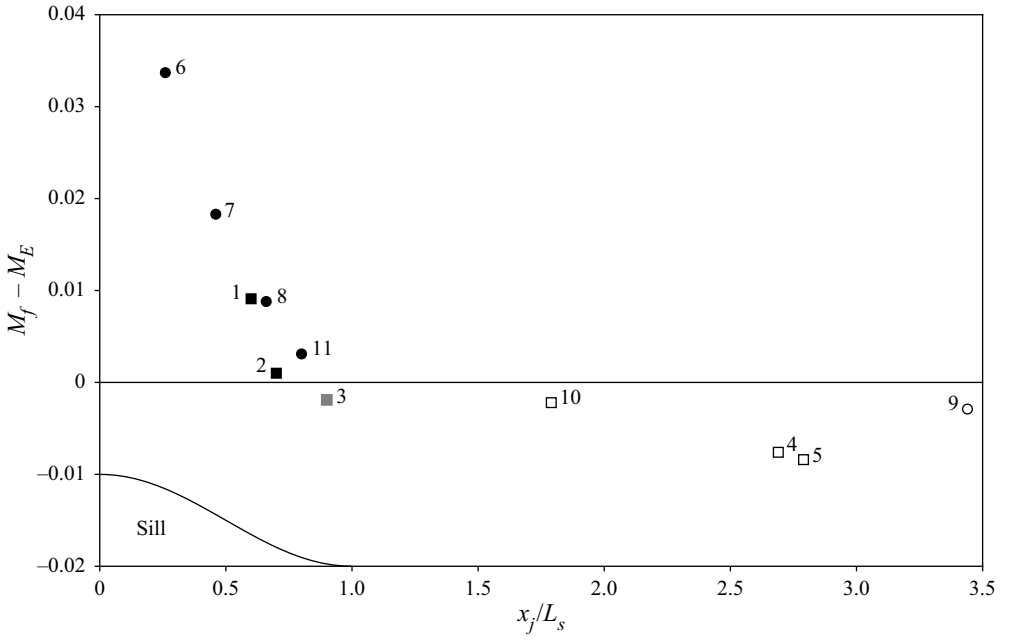

Figure 7. Value of $M_f - M_E$ plotted as a function of the normalised position of our internal hydraulic jumps, x_j/L_S, where x_j is the distance from the sill crest to the nose of the jump, and L_S is the half-width of the sill. The square symbols represent flows with $r = 0.33$; the circular symbols represent flows with $r = 0.4$; the solid symbols represent drowned jumps; the grey symbol represents a transitional jump; and the open symbols represent free jumps.

jumps (Exps. 6–8, figure 6*a–c*) the only deviation from a two-layer downstream density profile was an approximately linear reduction in density in the upper portion of the lower layer. The reduction in density across this linear region increased as the jump moved downstream, consistent with the hypothesis that as the jump moves downstream more upper layer fluid is entrained into it. The density profile downstream of the free jump (Exp. 9, figure 6*d*) had a different form; it was broader and more symmetric, more like the hyperbolic tangent profiles characteristic of mixing layers. This suggests that most of the mixing occurs in the shear layer upstream of the free jump. These observations are consistent with those of Wilkinson & Wood (1971), where the amount of entrainment and mixing was strongly impacted by jump position.

In all of the Series A and Series B experiments the jump location is consistent with the predictions of (2.22): i.e. when $M_E < M_f$, a drowned jump forms; when $M_E > M_f$ a free jump forms; and when $M_E \approx M_f$ a transitional jump forms near the end of the sill (figure 7). The sensitivity of the jump location to the value of $M_E - M_f$ is greater for free jumps than for drowned jumps as anticipated.

4. Mixing in internal hydraulic jumps

While the flows discussed above did not focus on mixing between the layers, they provide ample evidence of it. In figure 3(*a*) the lower layer (dyed red) and the upper layer (dyed blue) are distinct upstream of the obstacle, with a thin zone of mixed (purple) fluid at the interface. Downstream of the obstacle this zone of mixed fluid expands, particularly in the jump. Similarly, in Exps. 1–8 (figures 5 and 6*a–c*) a thin filament of dye injected at the interface at the upstream end of the channel expands to occupy most of the lower layer

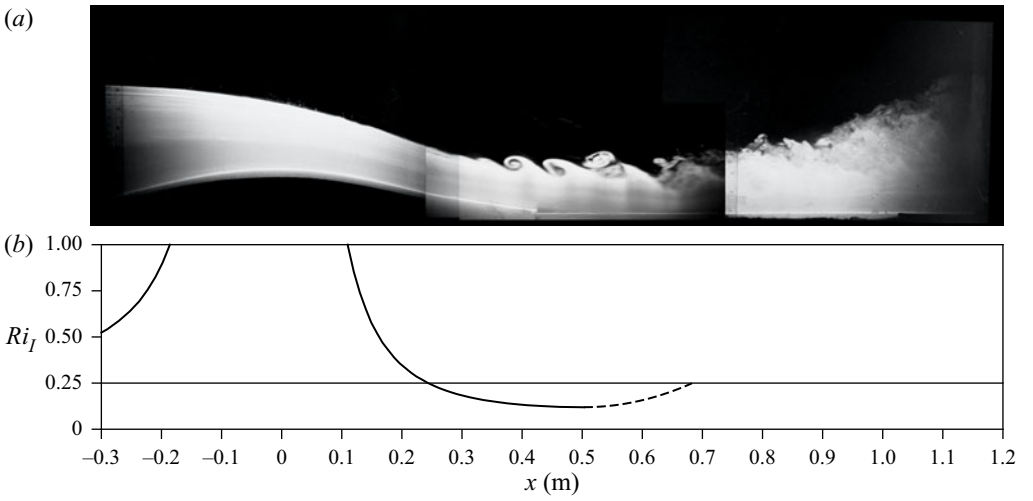

Figure 8. (*a*) Photographs of Exp. 10 showing the growth of Kelvin–Helmholtz instabilities on the interface as the lower layer accelerates down the lee slope of the obstacle. The flow was illuminated with a sheet of laser light aligned with the centre of the flume. The laser light causes sodium fluorescein dissolved in the lower layer to fluoresce. (*b*) The longitudinal variation in the interfacial Richardson number (Ri_I) based on an estimated upstream vorticity thickness of 0.6 cm and density interface thickness of 0.3 cm. Downstream of the crest the lower layer accelerates, Ri_I drops below 0.25, and the interface becomes unstable to Kelvin–Helmholtz instabilities.

downstream of the jump. The density profiles taken downstream of the jump in Exps. 6–9 (figure 6) show a reduction in the density of the upper portion of the lower layer. Finally, in several of the experiments (e.g. Exps. 1, 3, 6 and 7) Kelvin–Helmholtz billows are distinctly visible over the lee face of the sill.

4.1. *Shear instabilities*

Experiments 10 and 11 were performed to visualise the growth and fate of shear instabilities, and the turbulence and mixing associated with them, see figures 8 and 9. The parameters of Exp. 10 ($r = 0.33$, $G_0^2 = 0.39$ and $\beta_m = 0.21$) were intermediate between those of Exps. 3 and 4 (closer to Exp. 3), and a free jump formed downstream of the end of the sill. The parameters of Exp. 11 ($r = 0.40$, $G_0^2 = 0.36$ and $\beta_m = 0.19$) were intermediate between those of Exps. 8 and 9 (closer to Exp. 8), and a drowned jump formed near the end of the sill.

The laser imaging of Exp. 10 shows the growth of Kelvin–Helmholtz instabilities on the interface as the lower layer accelerates down the lee slope of the obstacle (figure 8*a*). Wavelike disturbances precede the appearance of two isolated billows and two billows in the process of pairing (figure 8*a*). These observations are consistent with the theory of the hydrodynamic stability of stratified shear flows. In this experiment, the velocity shear is centred about the density interface, so the gradient Richardson number at the density interface is given by

$$Ri_I = \frac{g'\delta_V^2}{(\Delta u)^2\,\delta_\rho}, \tag{4.1}$$

where the vorticity thickness, $\delta_V = \Delta U/(\partial u/\partial z)_I$, the density interface thickness, $\delta_\rho = -\Delta\rho/(\partial\rho/\partial z)_I$, where $\Delta u = u_2 - u_1$ and $\Delta\rho = \rho_2 - \rho_1$. The longitudinal variation of

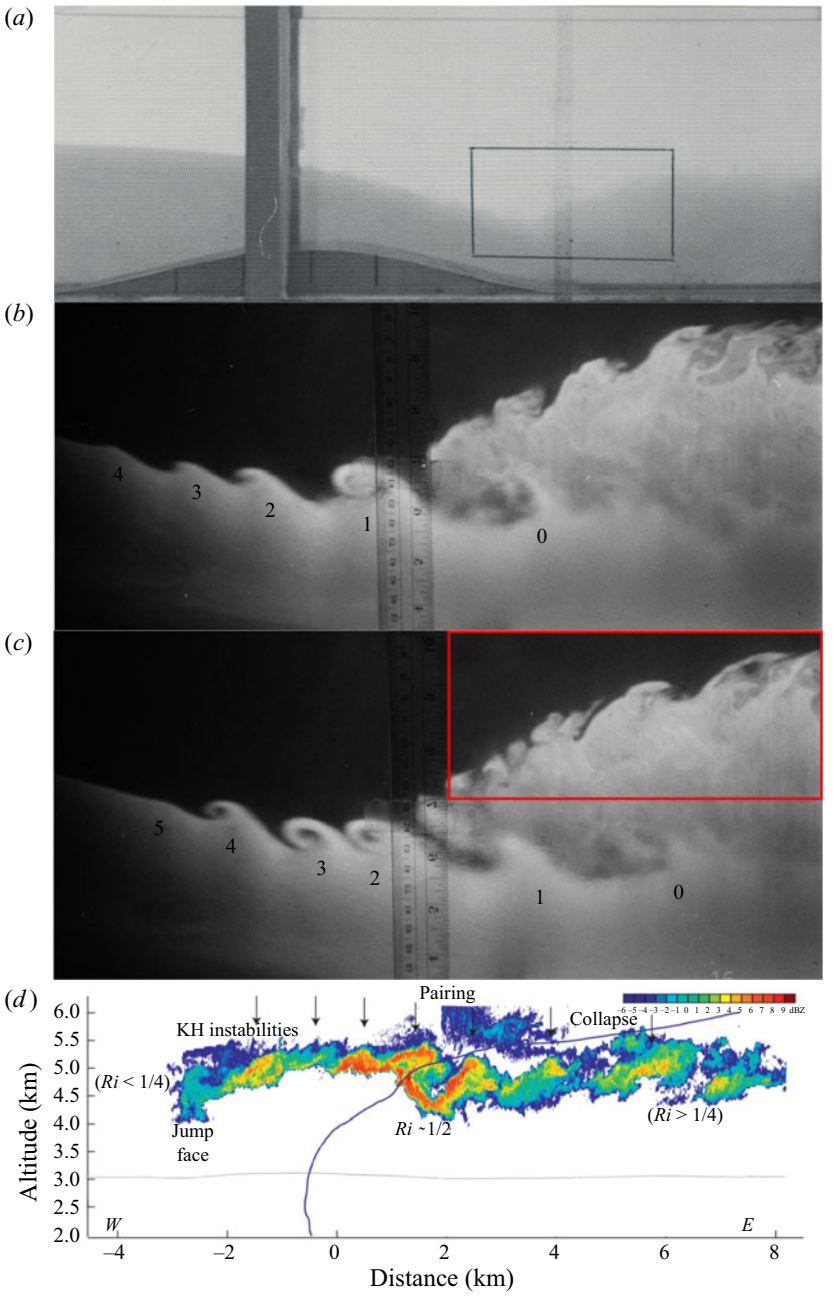

Figure 9. (*a–c*) Photographs of Exp. 11 demonstrating the formation and fate of Kelvin–Helmholtz billows. The flow was illuminated with a sheet of laser light aligned along the centreline of the flume. The laser light causes a dye dissolved in the lower layer to fluoresce. The region outlined in (*a*) is expanded in (*b*,*c*), which are successive photographs, taken 0.29 seconds apart. The growth and advection of a series of Kelvin–Helmholtz billows originating on the density interface in the supercritical flow upstream of the jump (denoted 1–4) is shown. These billows entrain fluid from the upper layer into the lower layer as they are advected beneath the jump. Billows (2) and (3) are in the process of pairing. An additional, weaker series of billows forms on the interface between the jump face and the upper layer (inside red box). Features in the red box are compared with (*d*), which is a radar image of the upper portion of an atmospheric internal hydraulic jump in the lee of the Sierra Nevada mountain range. Shear instabilities that form on the jump face, grow, pair and collapse as they are advected downstream. Adapted from Armi & Mayr (2011).

Ri_I is plotted in figure 8(*b*), using $\delta_V = 0.6$ and $\delta_\rho = 0.3$ cm, which are the values obtained from upstream velocity and density profiles. The variation of ΔU is calculated using the observed layer thicknesses and measured flow rates. Upstream of the obstacle $Ri_I > 0.25$ and the interface is stable, as predicted (Miles 1961; Corcos & Sherman 1976). As the flow passes over the obstacle ΔU initially decreases, until close to the crest both layers have the same flow speed, and $Ri_I \to \infty$. On the lee face of the obstacle the lower layer accelerates and Ri_I decreases until at about $x = 0.25$ m, Ri_I drops below 0.25. From this point, until the end of the sill, the flow becomes increasingly unstable and Kelvin–Helmholtz billows begin to grow. By the end of the sill, Ri_I is sufficiently low for the billows to pair (Koop & Browand 1979). An example of leapfrog pairing (Pawlak & Armi 1998; Thorpe 2007) is visible at $x \approx 0.5$ m in figure 8(*a*). After pairing, Ri_I increases to approximately 0.25 and further pairing is not observed.

4.2. *Structure of internal hydraulic jumps*

In Exp. 11 a drowned jump formed near the end of the sill (figure 9*a*), and the interaction of the flow upstream of the jump with the jump is captured in two photographs taken 0.29 s apart (figure 9*b*,*c*). In figure 9(*b*), billow '1' is located just upstream of the nose of the jump. Immediately, downstream of this billow is a parcel of upper layer fluid that has been drawn underneath the nose of the jump by the strain field of the previous billow '0'. As billow '1' advects beneath the nose of the jump, the parcel of upper layer fluid between '0' and '1' is fully entrained beneath the jump (figure 9*c*). Subsequently, this entrained fluid mixes with the jump fluid sitting above it. Similarly, we see that the parcel of upper layer fluid between billows '1' and '2' is drawn into the jump (figure 9*c*). Billows '2' and '3' grow between figures 9(*b*) and 9(*c*) and are in the process of pairing. Billow '4' is just starting to form in figure 9(*b*), but 0.29 seconds later, in figure 9(*c*), it is clearly visible. Billow '5' is starting to form in figure 9(*c*). Thus, there is a continuous train of billows that results in the entrainment of successive pulses of upper layer fluid into the jump. This is the primary source of entrainment and mixing associated with the jump.

Another potential source of mixing is a second set of billows that forms on the interface between the jump and the upper layer – the jump face, starting at the ruler in figure 9(*b*,*c*). These billows are subject to much less shear than the billows advecting beneath the jump, and do not cause as much entrainment and mixing. An atmospheric analogue of these billows has been observed on the face of the jump that forms in the lee of the Sierra Nevada mountain range shown in figure 9(*d*) (Armi & Mayr 2011). Although the shear Reynolds number, $Re^* \equiv \Delta u \delta_V / \nu \approx 1100$, is relatively high for a laboratory experiment, it dwarfs in comparison with the estimate of $O\left(10^9\right)$, for the case shown in figure 9(*d*). The observations are remarkably similar; in each case the billows grow, pair and collapse as they are advected downstream.

The unprecedented detail in figure 9(*d*) was captured by the University of Wyoming King Air research aircraft flying at 3.1 km with the radar looking upward beneath the internal hydraulic jump. Upstream is to the left, and the start of the cloud on the jump face is only visible when the streamlines rise to the lifted condensation level. The distance scale is centred in the valley at the town of Independence, California ($x = 0$ km). At the start of the jump face ($x \approx -2.7$ km), $Ri < 0.25$ and the flow is subject to instabilities that grow into vortices. The vortex at $x \approx -1.5$ km has entrained high-reflectivity (4 dBZ) moist air from below and wrapped it around its core. The next core centred at $x \approx -0.5$ km is less distinct, but the vortex centred at $x \approx 0.5$ km east has a clear mass of high reflectivity (5 dBZ) mixed throughout its core. The next two vortices downstream at $x \approx 1.5$ and $x \approx 2.5$ km east appear to be pairing, a process first clearly identified for unstratified

flows by Winant & Browand (1974) and Brown & Roshko (1974), as the mechanism for growth of a shear layer. Note that in stratified flows the pairing doubles the Richardson number, as recognised by Koop & Browand (1979). When the $Ri \gtrsim 0.25$ pairing is no longer possible and the coherent structures collapse, as can be seen in figure 9(*b–d*). The above observations are also consistent with data obtained from a balloon sounding that was launched from the ground at Independence and crossed the shear region at an altitude of 4.9 km (blue line in figure 9*d*). The Richardson number computed from the sounding was $Ri \approx 0.5$, therefore, downstream of the sounding no further growth of the shear layer is possible and the coherent structures collapse.

Experiments 12 and 13 were performed to further illustrate the dynamics of internal hydraulic jumps. In these experiments a higher flow rate ratio, $r = 0.50$, and a larger sill, $h_m = 15$ cm, were used to generate bigger jumps that could be measured in more detail. In Exp. 12 ($r = 0.50$, $G_0^2 = 0.31$ and $\beta_m = 0.37$), a drowned internal hydraulic jump formed approximately mid-way down the lee face of the sill (figure 10*a*). A series of vertical conductivity profiles were taken at $x = -1.0$, 1.0 and 3.0 m (figure 10*b–d*). The upstream profile shows the strongly two-layered upstream flow, where the density interface is about 3 mm thick (figure 10*b*). The profile at $x = 1.0$ m (just beyond the end of the sill) illustrates the vertical structure of the jump (figure 10*c*). For the purpose of discussion we identify five regions at this location, descending from the free surface:

(*A*) The upper layer in which the density remains constant at ρ_1.
(*B*) The shear layer on the jump face.
(*C*) The internal hydraulic jump, characterised by small amplitude fluctuations of variable frequency. This portion of the jump is buffeted by the shear layers above and below it.
(*D*) The shear layer at the base of the jump, consisting of a series of billows that were initiated upstream of the jump and advected beneath it. At $x = 1$ m this shear layer exhibits rapid and large fluctuations in conductivity, reflective of the passage of Kelvin–Helmholtz billows that have begun to break down. Here, the conductivity fluctuations are larger than those seen in the shear layer on the jump face (Region B), since the velocity shear and resultant instabilities are stronger.
(*E*) An undisturbed region of the lower layer into which shear instabilities do not penetrate. In this region the density remains constant at ρ_2.

Downstream of the jump, at $x = 3.0$ m, the flow has returned to being almost two-layered (figure 10*d*). The upper layer and the lower portion of the lower layer remain undisturbed. The billows on the jump face have broken down and collapsed leaving a sharp density interface approximately 1 cm thick. The shear layer at the base of the jump has merged with the jump to form a region of almost linear density gradient (figure 10*d*), and almost constant shear (not shown, but similar to figure 6*b*); we shall refer to this region as the jump wake. The average gradient Richardson number in this linearly stratified region is approximately 1.0, and there is no longer any shear instability, or active mixing. There are, however, still small density fluctuations that reflect incomplete mixing in the jump.

4.3. *Quantitative analysis of entrainment into internal hydraulic jumps*

In Exp. 13 ($r = 0.50$, $G_0^2 = 0.45$ and $\beta_m = 0.32$) a drowned jump formed near the end of the sill ($x = 0.9$ m). In this experiment we collected times series of conductivity (converted to density) at 23 vertical elevations at $x = 1.5$ m; 0.6 m downstream of the nose of the jump. Each time series consisted of 1024 measurements taken at 25 Hz.

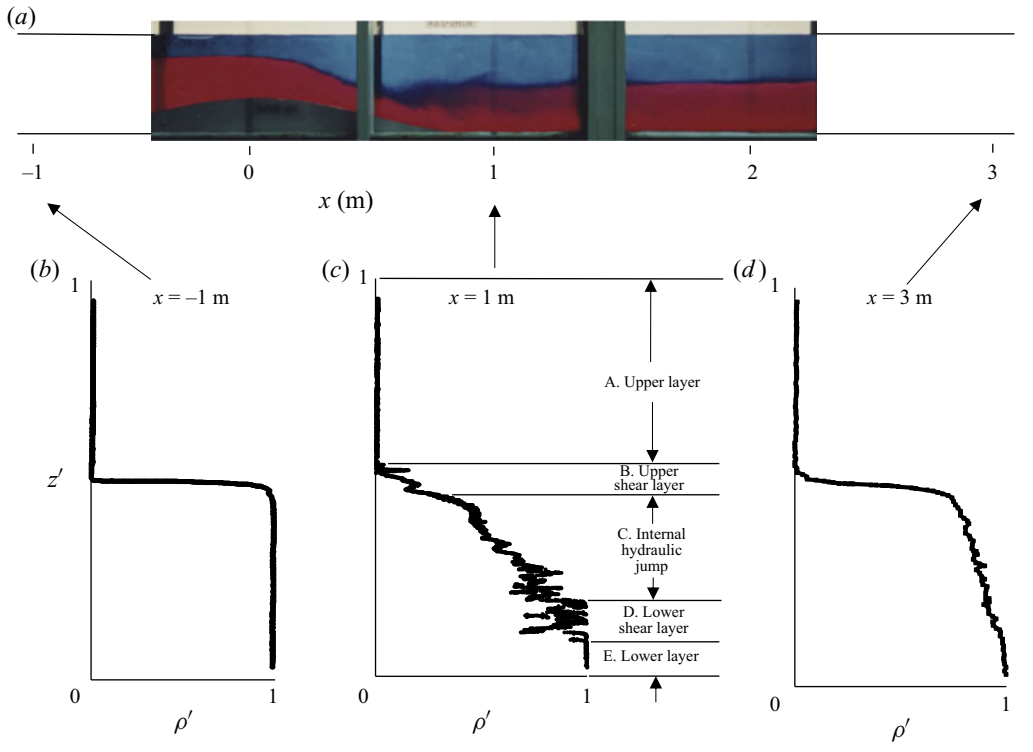

Figure 10. (*a*) Photograph of Exp. 12, (*b*) density profile at $x = -1$ m, (*c*) density profile at $x = 1$ m, (*d*) density profile at $x = 3$ m. Each profile took approximately 60 s to complete.

The non-dimensional density

$$\rho'(z') = \frac{\rho(z') - \rho_1}{\Delta\rho}, \tag{4.2}$$

where $z' = z/Y_0$, is plotted as a function of elevation in figure 11(*b*) for each of the 23 time series. This plot illustrates both the mean vertical density profile and the fluctuations about it. Five time series, representative of each of the five regions, are presented in figure 11(*a*). In the upper layer (Region A, e.g. $z' = 0.60$) the density is constant, except for instrumental noise, and equal to the density of the inflowing fresh water, $\rho' = 0$. In the upper shear layer (Region B, e.g. $z' = 0.48$), the density fluctuates in the range $0 \leq \rho' \leq 0.32$ due to the passage of pulses of entrained fluid that have been partially mixed into the shear layer. At this location billows are in the process of merging and this is reflected in the variable time scales of the density fluctuations. In the internal hydraulic jump (Region C, e.g. $z' = 0.42$), the density fluctuates slowly in the range $0.32 \leq \rho' \leq 0.64$: the passage of billows in both the upper and lower shear layers forcing the jump fluid up and down. In the lower shear layer (Region D, e.g. $z' = 0.22$) the density fluctuates in the range $0.64 \leq \rho' \leq 1$: these fluctuations are larger, and fluctuate more rapidly, than those in the upper shear layer, reflecting the more active mixing in the lower shear layer. In the lower layer (Region E, e.g. $z' = 0.06$) the density is constant, except for instrumental noise, and equal to the density of the inflowing saline water, $\rho' = 1$.

The density profiles presented in figure 10 show that the sharp two-layer flow observed upstream of the sill is substantially modified as it passes over the sill and through the jump. However, these profiles alone do not allow us to make quantitative estimates of the

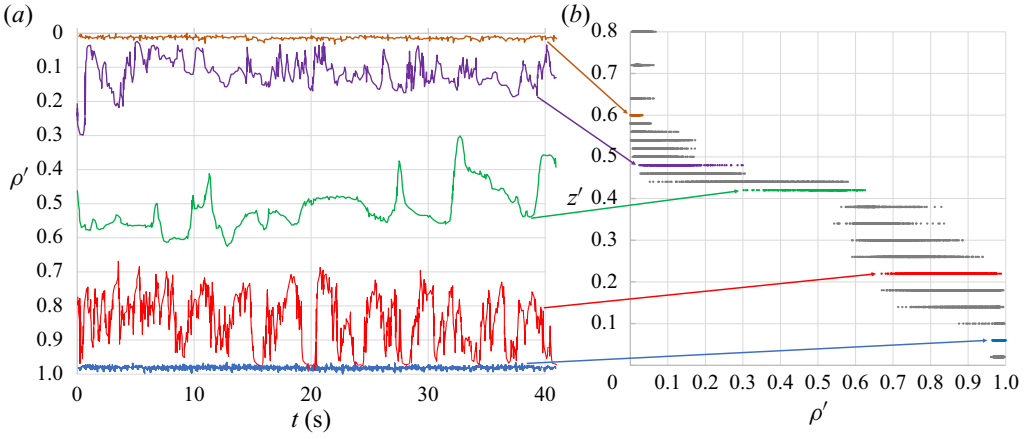

Figure 11. (*a*) Time series of density in Exp. 13 at $z = 0.06$, 0.22, 0.42, 0.48 and 0.60. (*b*) Compilations of density measurements at each location. Each time series consists of 1024 measurements taken at 25 Hz.

amount of entrainment and mixing that has occurred, because the velocity profiles have also changed. Both the velocity and density profiles need to be taken into account, and the appropriate way to do so is to compare normalised profiles of density as a function of streamfunction,

$$\psi(z') = \left\{ \int_0^{z'} u \, \mathrm{d}z' \right\} \frac{Y_0}{q}. \tag{4.3}$$

Here, we examine the profiles of ρ' vs ψ for experiments 6–9, see figure 12. The upstream ($x = -1.5$ m) profile for Exp. 6 is indistinguishable from the upstream profiles for Exps. 7–9 (not shown), demonstrating the two-layer nature of the upstream flow. For each experiment, profiles were taken sufficiently far downstream of the jump ($x = 4.5$ m) for active mixing to have ceased. The gradient Richardson number in the wake of the jump is of $O(1)$ in each case.

The density-streamfunction profiles highlight the differences between free jumps and drowned jumps with respect to entrainment and mixing. In the drowned jumps (Exps. 6–8), a considerable amount of upper layer fluid is entrained and mixed into the lower layer, but almost no fluid from the lower layer is mixed into the upper layer (figure 12*a*). In the free jump (Exp. 9), mixing occurs almost symmetrically about the interface (figure 12*b*). To quantify entrainment rates we define the flux of upper layer fluid entrained into the lower layer as

$$q_{12} = \int_0^{\psi_{INT}} \left(1 - \rho'\right) \mathrm{d}\psi, \tag{4.4}$$

and the flux of lower layer fluid entrained into the upper layer as

$$q_{21} = \int_{\psi_{INT}}^{1} \rho' \mathrm{d}\psi, \tag{4.5}$$

where we define ψ_{INT} is the value of the streamfunction when $\rho' = r$. The net entrainment flux

$$q_{ENT} = q_{12} - q_{21}. \tag{4.6}$$

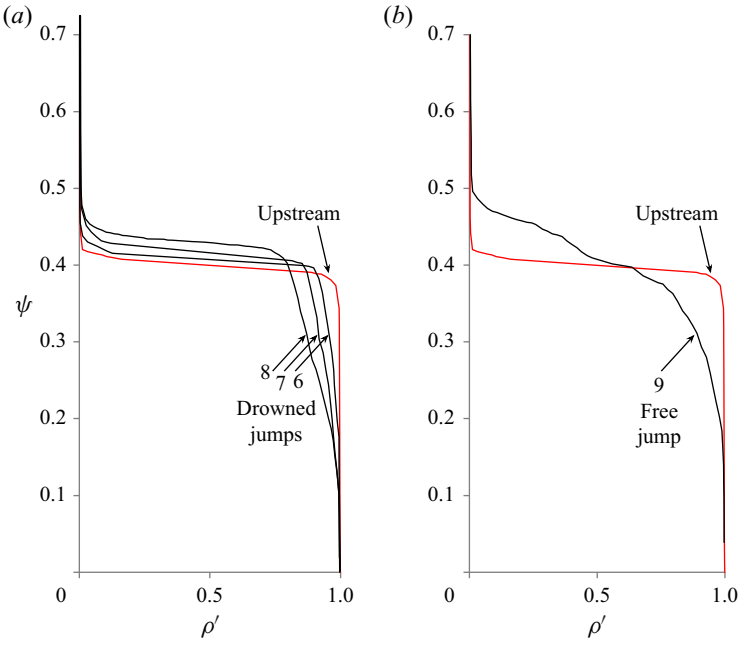

Figure 12. (*a*) Profile of ρ' vs ψ upstream ($x = -1.5\,m$) of the sill in Exp. 6 (red), and profiles of ρ' vs ψ downstream ($x = 4.5$ m) of the drowned jumps in Exps. 6–8 (black). (*b*) Profile of ρ' vs ψ upstream ($x = -1.5$ m) of the sill in Exp. 9 (red), and profiles of ρ' vs ψ downstream ($x = 4.5$ m) of the free jump in Exps. 9 (black).

Note that combining (4.4) and (4.5), and recognising that $\int_0^1 \rho'\,\mathrm{d}\psi = r$, gives

$$q_{ENT} = \psi_{INT} - r. \tag{4.7}$$

The values of q_{12}, q_{21}, q_{ENT} and ψ_{INT} for each of the profiles are given in table 2.

The profile obtained at $x = -1.5$ m in Exp. 6, is typical of the upstream profile in all experiments, and shows an almost perfectly two-layered flow (figure 12*a*): very little fluid has been entrained across the interface in either direction, see table 2. The lack of entrainment reflects the care taken to minimise mixing upstream: in the channel upstream of the sill the interfacial Richardson number, $Ri_I = O(0.5)$, see figure 8(*b*). The distinctly two-layer flow upstream of the sill allows us to focus on the mixing and entrainment associated with the jump, and their impact on the downstream flow. We discuss the experiments with drowned jumps first (Exps. 6–8), and then the experiment with a free jump (Exp. 9).

In the case of drowned jumps (Exps. 6–8), far more fluid is entrained from the upper layer into the lower layer, than *vice versa*, i.e. $q_{12} \gg q_{21}$ (table 2). In fact, within the accuracy of our experiments, $q_{21} = 0.004$ is the same as it was upstream of the sill, indicating that there is a negligible amount of mixing caused by the upper shear layer in drowned jumps, consistent with figure 6(*a–c*). The amount of fluid entrained and mixed by the lower shear layer increases as a drowned jump moves down the lee face of the sill, see figure 13 and table 2. The further downstream that a jump forms, the greater the length of the shear layer that is exposed upstream of the jump, and the more entrainment into the jump. This increasing entrainment is reflected in the increasing density deficit downstream of the jump (figure 12*a*). Beneath the jump the shear layer is subject to pairing, and continues to grow until it occupies the full depth of the wake of the jump. Downstream

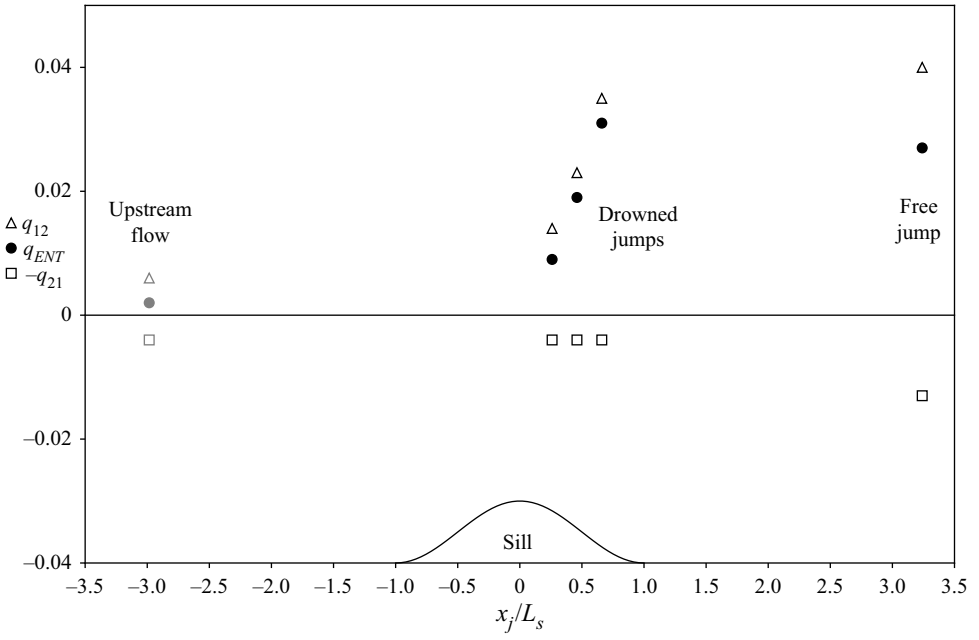

Figure 13. Entrainment fluxes downstream ($x = 4.5$ m) of the jump in Exps. 6–9 plotted against the normalised jump location, x_j/L_S. The open triangles represent, q_{12}, the flux of fresh fluid in the lower layer; the open squares represent, $-q_{21}$, and the closed circles represent the net entrainment flux, $q_{ENT} = q_{12} - q_{21}$. The grey symbols are from measurements taken upstream ($x = -1.5$ m) of the sill.

($x = 4.5$ m) of a drowned jump there is an almost linear decrease in ρ' with increasing ψ in the wake of the jump (figure 12*a*). The interface between the upper layer and the lower layer downstream of the jump remains sharp, confirming that the shear instabilities on the upper face of the jump do not result in a significant amount of mixing. Even though the lower shear layer is relatively strong, it is not strong enough to penetrate the bottom boundary layer, and the lower portion of the lower layer remains undisturbed.

In Exp. 9, in which a free jump forms far downstream of the sill, the behaviour is quite different. Immediately downstream of the sill $Ri \ll 0.25$ and billows pair: further downstream $Ri \gtrsim 0.25$, and they collapse and breakdown due to secondary three-dimensional instabilities. In the resulting mixed layer, the velocity and density profiles vary relatively smoothly. The jump that forms downstream of this mixed layer is more of a gradual expansion with no roller region (see figures 2(*a*), 5 and 6(*d*)), in contrast with the drowned jumps described above. Downstream of the free jump the $\psi(\rho')$ plot is almost symmetric about the interface, see figure 12(*b*). Thus, there is a dramatic difference between drowned jumps and free jumps, both in the structure of the jump and the entrainment and mixing associated with it.

In developing the theory presented in § 2 we assumed that the change in r due to entrainment into the jump was small. This assumption is satisfied in our experiments where the maximum value of $q_{ENT} \approx 0.031$ (Exp. 8), which is indeed small compared with $r = 0.4$. To achieve much greater entrainment, the velocity shear between the two layers upstream of the jump would have had to have been much greater, but this is not achievable in two-layer flow over a sill, where the driving force is the pressure difference due to a higher interface level upstream of the sill than downstream.

However, much higher velocity shears can be achieved in flows of the type studied by Wilkinson & Wood (1971), where the upstream flow was a strong boundary jet injected through a small (1 cm high) duct under high pressure. In the strong internal jumps of Wilkinson & Wood (1971), the shear internal Froude number (see Appendix A) at location E, $F^2_{\Delta E} = 50$–270; and the flux of ambient fluid entrained into the jet was up to 200 % of the initial jet flux.

While Wilkinson and Wood achieved high shear internal Froude numbers by discharging under pressure, consistent with engineering applications, the Froude numbers achieved in our experiments were limited by the difference in interface height upstream and downstream of the sill, as is also the case in geophysical flows (e.g. Mayr & Armi 2008). In our experiments $F^2_{2E} = 2.9$–4.0, see table 1. Even though the density and velocity profiles were modified upstream and downstream of the jump, a sharp density interface persisted downstream of the jump. In Exp. 9 the flux of upper layer fluid entrained into the lower layer, $q_{12} = 0.04$ (table 2) was 10 % of the initial lower layer flux; i.e. $q_{12}/r = 0.1$, see table 2. This value, the highest achieved in our experiments, is more than an order of magnitude less than the entrainment rates of Wilkinson & Wood (1971).

5. Summary and conclusions

Our laboratory experiments were conducted to investigate the hydraulics of, and mixing associated with, stationary internal hydraulic jumps in high Reynolds number two-layer flows. In these experiments a layer of fresh water overlying a layer of salt water flowed through a long rectangular channel with a horizontal bed. An underwater sill was installed approximately midway along the channel to generate internally supercritical flow downstream of its crest. A contraction, of adjustable width, was installed at the downstream end of the channel. This contraction ensured internally subcritical flow with approximately equal velocity in each layer at its entrance. It also controlled the total depth of flow within the flume. The transition from internally supercritical flows to internally sub-critical downstream flows was achieved via internal hydraulic jumps. Our experimental set-up is unique in that it models stationary internal hydraulic jumps in barotropically driven two-layer flows over a fixed obstacle, as might occur in tidally driven flows over underwater sills, or flows over mountains driven by large-scale pressure gradients.

Our analysis of internal hydraulic jumps closely follows that of free-surface hydraulic jumps. A two-layer momentum function for two-layer flows is derived specifically for our experimental configuration. For flow with an internal hydraulic jump at the end of the sill (transitional jump), the momentum at the end of the sill, M_E, is equal to M_f, the frictional momentum loss between the end of the sill and the start of the downstream contraction. If $M_E < M_f$, a jump will form over the lee face of the sill (drowned jump), and if $M_E > M_f$, a jump will form downstream of the sill (free jump). Our experimental observations are consistent with these predictions.

The primary source of mixing in our experiments is a train of Kelvin–Helmholtz billows that forms on the interface between the two layers and grows as the lower layer accelerates down the lee face of the sill. Upper layer fluid is entrained into these billows, and is advected downstream with them. The subsequent evolution of the flow depends upon the location of the jump. In the case of drowned jumps over the lee face of the sill, the billows are still growing, and possibly pairing, as they approach the jump. As each billow is advected beneath the nose of the internal hydraulic jump, the upper layer fluid entrained into the billow is also advected into the jump. Thus, periodic pulses of entrained upper layer fluid enter the jump. Once within the jump, this entrained fluid mixes with the jump

fluid sitting above it. Downstream of the jump, the upper layer remains homogeneous and a sharp density step at the interface persists. As a result of entrainment into, and mixing within, the jump, the upper portion of the lower layer is approximately linearly stratified and the lower portion remains undisturbed. A second, upper shear layer, between the undisturbed upper layer and the top of the internal hydraulic jump, has minimal impact on the downstream density profile.

If a free jump forms sufficiently far downstream of the sill, the flow evolves differently. The lower layer will stop accelerating once it reaches the end of the sill. Initially the billows will continue to grow, but as the Richardson number increases, these billows will collapse and breakdown due to secondary, three-dimensional instabilities. In the resulting mixed layer the velocity and density profiles vary relatively smoothly. The jump that forms downstream of this mixed layer is more of a gradual expansion with no roller region, and downstream of the jump a broad density interface persists.

Thus, the amount of entrainment and mixing associated with an internal hydraulic jump, and shape of the density profile downstream of it, are strongly dependent on the location of the jump relative to the sill: the length of the shear layer upstream of the jump governs the evolution of the flow.

Acknowledgements. The authors are grateful to G. Corcos, D. Farmer, H. Fischer and S. Monismith for insight and inspiration. C. White and A. Law helped with the experiments. D. Robb, R. Pieters, M. Tong and P. Chen assisted with preparation of this manuscript.

Funding. Our research was funded by the Natural Sciences and Engineering Research Council of Canada, the US National Science Foundation and Lucky Larry's Auto Repair.

Declaration of interests. The authors report no conflict of interest.

Author ORCIDs.
Gregory A. Lawrence https://orcid.org/0000-0002-1011-8227.

Appendix A. Appropriate downstream geometry for study of internal hydraulic jumps

Here, we examine the suitability of two simple downstream geometries, an underwater sill and a contraction, for the study of internal hydraulic jumps in the laboratory. Immediately downstream of an internal hydraulic jump the flow is both internally and, of course, externally subcritical. Before exiting the channel this flow is subject to two controls: the first controlling the interface elevation, where the internal Froude number

$$F_I^2 = \frac{(u_1 y_2 + u_2 y_1)^2}{g' Y y_1 y_2 \left(1 - F_\Delta^2\right)} = 1, \tag{A1}$$

see Lawrence (1990); and the second, located further downstream, controlling the free surface height, where the external Froude number

$$F_E^2 = \frac{u^2}{gY} = 1, \tag{A2}$$

and $u = q/Y$. In many studies of internal hydraulics, the composite Froude number

$$G^2 = F_1^2 + F_2^2 + \varepsilon F_1^2 F_2^2, \tag{A3}$$

see Armi (1986), is invoked to specify the criticality of two-layer flows. This approach is valid since

$$1 - G^2 = (1 - F_I^2)(1 - F_E^2)(1 - F_\Delta^2), \tag{A4}$$

see Lawrence (1990). Note that the results presented here are only valid if Long's (1956) criterion, $F_\Delta^2 < 1$, is satisfied, which is the case in all of our experiments.

A.1. *Flow over an underwater sill*

For steady two-layer flow over an underwater sill at the end of a horizontal channel of constant width, the streamwise variation in free surface elevation

$$\frac{\mathrm{d}Y}{\mathrm{d}x} = \frac{\varepsilon F_1^2 F_2^2}{1 - G^2}\frac{\mathrm{d}h}{\mathrm{d}x}, \tag{A5}$$

see Armi (1986). Therefore, from (A4) and (A5), if the sill is sufficiently high, an external control, $F_E^2 = 1$, occurs at the crest of the sill, where $\mathrm{d}h/\mathrm{d}x = 0$. The streamwise variation in the interface elevation, $y_{INT} = y_2 + h$, is given by

$$\frac{\mathrm{d}y_{INT}}{\mathrm{d}x} = -\frac{F_2^2\left(1 - \varepsilon \mathrm{F}_1^2\right)}{1 - G^2}\frac{\mathrm{d}h}{\mathrm{d}x}, \tag{A6}$$

see Armi (1986). There are two alternative scenarios. In the first scenario, there is no internal hydraulic control and the flow is internally supercritical, both as it approaches the sill and as it flows over it; there can be no internal hydraulic jump. In the second scenario, an internal hydraulic control, known as an approach control (Lawrence 1993), is located at the start of the sill, where $\mathrm{d}h/\mathrm{d}x = 0$. An internal hydraulic jump is theoretically possible in this scenario, but it would have to form far upstream of the downstream sill to allow frictional effects enough distance to transform the flow from the conjugate internally subcritical state downstream of the jump to the internally critical flow at the start of the sill. Unfortunately, the channel would need to be prohibitively long to achieve this second scenario, and an underwater sill at the end of the channel is not suitable for studying internal hydraulic jumps.

A.2. *Flow through a contraction*

For steady two-layer flow through a contraction at the end of a horizontal channel of constant width, see figure 4, the streamwise variation in the thickness of the layers passing through the contraction is given by

$$\frac{\mathrm{d}y_1}{\mathrm{d}x} = \left[\frac{G^2 - (1 + y_2/y_1)\,F_2^2}{1 - G^2}\right]\frac{y_1}{w}\frac{\mathrm{d}w}{\mathrm{d}x}, \tag{A7a}$$

$$\frac{\mathrm{d}y_2}{\mathrm{d}x} = \left[\frac{G^2 - (1 + ry_1/y_2)\,F_1^2}{1 - G^2}\right]\frac{y_2}{w}\frac{\mathrm{d}w}{\mathrm{d}x}, \tag{A7b}$$

where w is the width of the channel (Armi 1986). These equations are fundamentally different from those for flow over a sill in that hydraulic controls do not have to occur at a topographic constraint ($\mathrm{d}w/\mathrm{d}x = 0$). They can also occur when

$$1 - \left(1 + \frac{y_2}{y_1}\right)F_2^2 = 0 \quad \text{and} \quad 1 - \left(1 + \frac{ry_1}{y_2}\right)F_1^2 = 0 \tag{A8a,b}$$

which requires, that for $\varepsilon \ll 1$:

$$u_1^2 = u_2^2. \tag{A9}$$

Wood (1968) called such controls 'virtual' controls. His analysis applies to two-layer flows entering a contraction; as the contraction narrows these flows accelerate, first passing

through an internal 'virtual' control within the contraction, and then through an external control at the end of the channel. The flow upstream of the entrance to the contraction can be sufficiently internally subcritical that, an internal hydraulic jump can form a short distance upstream of it.

A downstream contraction in combination with an upstream underwater sill is shown in figure 4. An internally supercritical flow can form downstream of the crest of the sill, and an approximately uniform internally subcritical flow forms upstream of the contraction. The flow transitions between these two regimes via an internal hydraulic jump, with an approximately uniform downstream velocity profile, which is the desired scenario for the present study.

References

Arita, M., Jirka, G.H. & Tamai, N. 1986 Classification and mixing of two-dimensional buoyant surface discharges. *J. Hydraul Res.* **24** (5), 333–345.

Armi, L. 1986 The hydraulics of two flowing layers with different densities. *J. Fluid Mech.* **163**, 27–58.

Armi, L. & Farmer, D.M. 1988 The flow of Mediterranean water through the Strait of Gibraltar. *Prog. Oceanogr.* **21** (1), 1–105.

Armi, L. & Mayr, G. 2011 The descending stratified flow and internal hydraulic jump in the lee of the Sierras. *J. Appl. Meteorol. Climatol.* **50** (10), 1995–2011.

Baddour, R.E. 1987 Hydraulics of shallow and stratified mixing channel. *J. Hydraul.Engng* **113** (5), 630–645.

Baddour, R.E. & Abbink, H. 1983 Turbulent underflow in a short channel of limited depth. *J. Hydraul.Engng* **109** (5), 722–740.

Baines, P.G. 1984 A unified description of two-layer flow over topography. *J. Fluid Mech.* **146**, 127–167.

Baines, P.G. 1995 *Topographic Effects in Stratified Flows*. Cambridge University Press.

Barahmand, N. & Shamsai, A. 2010 Experimental and theoretical study of density lumps on smooth and rough beds. *Lake. Reserv.* **15**, 285–306.

Bélanger, J.B. 1828 *Essai sur la solution numérique de quelques problèmes relatifs au mouvement permanent des eaux courantes (Essay on the Numerical Solution of Some Problems Relative to the Steady Flow of Water)*. Carilian-Goeury.

Borden, Z. & Meiburg, E. 2013 Circulation-based models for Boussinesq internal bores. *J. Fluid Mech.* **726**, R1.

Borden, Z., Meiburg, E. & Constantinescu, G. 2012 Internal bores: an improved model via a detailed analysis of the energy budget. *J. Fluid Mech.* **703**, 279–314.

Brown, G.L. & Roshko, A. 1974 On density effects and large scale structures in turbulent mixing layers. *J. Fluid Mech.* **64**, 775–816.

Chow, V.T. 1959 *Open Channel Hydraulics*. McGraw Hill.

Chu, V.H. & Baddour, R.E. 1977 Surges, waves and mixing in two-layer density stratified flow. In *Proc. 17th Congr. Intl. Assn. Hydraul. Res.*, vol. 1, pp. 303–310.

Colson, D. 1952 Results of double-theodolite observations at Bishop, Cal, in connection with the "Bishop-Wave" phenomena. *Bull. Am. Meteorol. Soc.* **33** (3), 107–116.

Corcos, G.M. & Sherman, F.S. 1976 Vorticity concentration and the dynamics of unstable free shear layers. *J. Fluid Mech.* **73**, 241–264.

Findikakis, A.N. & Law, W.K. 1998 Marine tailings disposal simulation. *J. Hydraul. Engng* **124**, 370–382.

Finnemore, E.J. & Franzini, J.B. 2002 *Fluid Mechanics*, 10th edn. McGraw-Hill.

Garcia, M. & Parker, G. 1989 Experiments on hydraulic jumps in turbidity currents near a canyon-fan transition. *Science* **245**, 393–396.

Guglielmini, D. 1697 *Della natura de' fiumi: Trattato fisico-matematico. (On the nature of rivers: A physical-mathematical treatise).* Per gl'Eredi d'Antonio Pisarri.

Hassid, S., Regev, A. & Poreh, M. 2007 Turbulent energy dissipation in density jumps. *J. Fluid Mech.* **572**, 1–12.

Henderson, F.M. 1966 *Open Channel Flow*, MacMillan Series in Civil Engineering. Macmillan.

Kite, H.D., Topham, D.R. & Van Hardenburg, B.J. 1995 Laboratory measurements of the drag force on a family of two-dimensional ice keel models in a two-layer flow. *J. Phys. Oceanogr.* **25**, 3008–3031.

Klemp, J.B., Rotunno, R. & Skamarock, W.C. 1997 On the propagation of internal bores. *J. Fluid Mech.* **331**, 81–106.

KOOP, C.G. & BROWAND, F.K. 1979 Instability and turbulence in a stratified fluid with shear. *J. Fluid Mech.* **93**, 135–159.

LAWRENCE, G.A. 1985 The hydraulics and mixing of two-layer flow over an obstacle. PhD Thesis and Report No. UCB/HEL-85/02, Hydraulic Engineering Laboratory, Department of Civil Engineering, University of California, Berkeley.

LAWRENCE, G.A. 1990 On the hydraulics of Boussinesq and non-Boussinesq two-layer flows. *J. Fluid Mech.* **215**, 457–480.

LAWRENCE, G.A. 1993 The hydraulics of steady two-layer flow over a fixed obstacle. *J. Fluid Mech.* **254**, 605–633.

LI, M. & CUMMINS, P.F. 1998 A note on hydraulic theory of internal bores. *Dyn. Atmos. Oceans* **28** (1), 1–7.

LONG, R.R. 1954 Some aspects of the flow of stratified fluids. II. Experiments with a two-fluid system. *Tellus* **6**, 97–115.

LONG, R.R. 1956 Long waves in a two-fluid system. *J. Meteorol.* **13**, 70–74.

LONG, R.R. 1972 Stratified Flow. 16 mm sound film and accompanying text in Illustrated Experiments in Fluid Mechanics: The NCFMF Book of Film Notes. Based on material in films produced under direction of the National Committee for Fluid Mechanics Films, MIT Press. http://web.mit.edu/hml/ncfmf.html.

MAYR, G.J. & ARMI, L. 2008 Föhn as a response to changing upstream and downstream air masses. *Q. J. R. Meteorol. Soc.* **134**, 1357–1369.

MILES, J.W. 1961 On the stability of heterogeneous shear flows. *J. Fluid Mech.* **10**, 496–508.

OGDEN, K.A. & HELFRICH, K.R. 2020 Internal hydraulic jumps in two-layer flows with increasing upstream shear. *Phys. Rev. Fluids* **5** (7), 074803.

PAWLAK, G. & ARMI, L. 1998 Vortex dynamics in a spatially accelerating shear layer. *J. Fluid Mech.* **376**, 1–35.

RAJARATNAM, N. & POWLEY, R.J. 1990 Hydraulic jumps in two-layer flows. *Proc. Inst. Engrs* **89** (2), 127–142.

RAJARATNAM, N. & SUBRAMANYAN, S. 1985 Plane turbulent buoyant surface jets and jumps. *J. Hydraul. Res.* **23** (2), 131–146.

RAJARATNAM, N. & SUBRAMANYAN, S. 1986 Plane turbulent denser wall jets and jumps. *J. Hydraul. Res.* **24** (4), 281–296.

ROTTMAN, J.W. & SIMPSON, J.E. 1989 The formation of internal bores in the atmosphere: a laboratory model. *Q. J. R. Meteorol. Soc.* **115** (488), 941–963.

ROTUNNO, R. & SMOLARKIEWICZ, P.K. 1995 Vorticity generation in the shallow-water equations as applied to hydraulic jumps. *J. Atmos. Sci.* **52** (3), 320–330.

STEFAN, H. & HAYAKAWA, N. 1972 Mixing induced by an internal hydraulic jump. *J. Am. Water Resour. Assoc.* **8** (3), 531–545.

THORPE, S., MALARKEY, J., VOET, G., ALFORD, M., GIRTON, J. & CARTER, G. 2018 Application of a model of internal hydraulic jumps. *J. Fluid Mech.* **834**, 125–148.

THORPE, S.A. 2007 *An Introduction to Ocean Turbulence*. Cambridge University Press.

THORPE, S.A. 2010 Turbulent hydraulic jumps in a stratified shear flow. *J. Fluid Mech.* **654**, 305–350.

THORPE, S.A. & LI, L. 2014 Turbulent hydraulic jumps in a stratified shear flow. Part 2. *J. Fluid Mech.* **758**, 94–120.

WESSON, J.C. & GREGG, M.C. 1994 Mixing at Camarinal Sill in the Strait of Gibraltar. *J. Geophys. Res.* **99** (C5), 9847–9878.

WILKINSON, D.L. 1970 Studies in density stratified flows. *Water Research Laboratory Rep. No.* 118. University of N.S.W.

WILKINSON, D.L. & WOOD, I.R. 1971 A rapidly varied flow phenomenon in a two-layer flow. *J. Fluid Mech.* **47** (2), 241–256.

WINANT, C.D. & BROWAND, F.K. 1974 Vortex pairing: the mechanism of turbulent mixing-layer growth at moderate Reynolds number. *J. Fluid Mech.* **63**, 237–255.

WOOD, I.R. 1968 Selective withdrawal from a stably stratified fluid. *J. Fluid Mech.* **32** (2), 209–223.

WOOD, I.R. & SIMPSON, J.E. 1984 Jumps in layered miscible fluids. *J. Fluid Mech.* **140**, 329–342.

YEH, H.H. 1991 Vorticity generation mechanisms in bores. *Proc. Roy. Soc.* A **432**, 215–231.

YIH, C-S. & GUHA, C.R. 1955 Hydraulic jump in a fluid system of two layers. *Tellus* **7** (3), 358–366.

ZHU, D.Z. & LAWRENCE, G.A. 1998 Non-hydrostatic effects in layered shallow water flows. *J. Fluid Mech.* **355**, 1–16.